

Cancellous bone and theropod dinosaur locomotion. Part III - Inferring posture and locomotor biomechanics in extinct theropods, and its evolution on the line to birds

Peter Bishop ^{Corresp. 1}, **Scott Hocknull** ¹, **Christofer Clemente** ², **John Hutchinson** ³, **Andrew Farke** ⁴, **Rod Barrett** ⁵, **David Lloyd** ⁵

¹ Geosciences Program, Queensland Museum, Brisbane, Queensland, Australia

² School of Science and Engineering, University of the Sunshine Coast, Maroochydore, Queensland, Australia

³ Department of Comparative Biomedical Sciences, Royal Veterinary College, Hatfield, Hertfordshire, United Kingdom

⁴ Raymond M. Alf Museum of Paleontology at The Webb Schools, Claremont, California, United States of America

⁵ School of Allied Health Sciences, Griffith University, Gold Coast, Queensland, Australia

Corresponding Author: Peter Bishop

Email address: peter.bishop@qm.qld.gov.au

This three-part series investigates the architecture of cancellous bone in the main hindlimb bones of theropod dinosaurs, and uses cancellous bone architectural patterns to infer locomotor biomechanics in extinct non-avian species. Cancellous bone is highly sensitive to its prevailing mechanical environment, and may therefore help further understanding of locomotor biomechanics in extinct tetrapod vertebrates such as dinosaurs. Here in Part III, the biomechanical modelling approach derived previously was applied to two species of extinct, non-avian theropods, *Daspletosaurus torosus* and *Troodon formosus*. Observed cancellous bone architectural patterns were linked with quasi-static, three-dimensional musculoskeletal and finite element models of the hindlimb of both species, and used to derive characteristic postures that best aligned continuum-level principal stresses with cancellous bone fabric. The posture identified for *Daspletosaurus* was largely upright, with a subvertical femoral orientation, whilst that identified for *Troodon* was more crouched, but not to the degree observed in extant birds. In addition to providing new insight on posture and limb articulation, this study also tested previous hypotheses of limb bone loading mechanics and muscular control strategies in non-avian theropods, and how these aspects evolved on the line to birds. The results support the hypothesis that an upright femoral posture is correlated with bending-dominant bone loading and abduction-based muscular support of the hip, whereas a crouched femoral posture is correlated with torsion-dominant bone loading and long-axis rotation-based muscular support. Moreover, the results of this study also support the inference that hindlimb posture, bone loading mechanics and muscular support strategies evolved in a gradual fashion along the line to extant birds.

1 Cancellous bone and theropod dinosaur locomotion.
2 Part III – Inferring posture and locomotor
3 biomechanics in extinct theropods, and its evolution
4 on the line to birds

5

6

7 P.J. Bishop^{1,2,3,*}, S.A. Hocknull^{1,2,3}, C.J. Clemente^{4,5}, J.R. Hutchinson⁶, A.A. Farke⁷, R.S.

8 Barrett^{2,3} and D.G. Lloyd^{2,3}.

9

10

11 ¹Geosciences Program, Queensland Museum, Brisbane, Queensland, Australia.

12 ²School of Allied Health Sciences, Griffith University, Gold Coast, Queensland, Australia.

13 ³Innovations in Health Technology, Menzies Health Institute Queensland.

14 ⁴School of Science and Engineering, University of the Sunshine Coast, Maroochydore,
15 Queensland, Australia.

16 ⁵School of Biological Sciences, The University of Queensland, Brisbane, Queensland, Australia.

17 ⁶Structure and Motion Laboratory, Department of Comparative Biomedical Sciences, Royal
18 Veterinary College, Hatfield, Hertfordshire, UK.

19 ⁷Raymond M. Alf Museum of Paleontology at The Webb Schools, Claremont, California, USA.

20

21 *corresponding author: peter.bishop@qm.qld.gov.au.

22

23

24

25

26

27

28

29 **III.1 Abstract**

30

31 This three-part series investigates the architecture of cancellous bone in the main hindlimb bones
32 of theropod dinosaurs, and uses cancellous bone architectural patterns to infer locomotor
33 biomechanics in extinct non-avian species. Cancellous bone is highly sensitive to its prevailing
34 mechanical environment, and may therefore help further understanding of locomotor
35 biomechanics in extinct tetrapod vertebrates such as dinosaurs. Here in Part III, the
36 biomechanical modelling approach derived previously was applied to two species of extinct, non-
37 avian theropods, *Daspletosaurus torosus* and *Troodon formosus*. Observed cancellous bone
38 architectural patterns were linked with quasi-static, three-dimensional musculoskeletal and finite
39 element models of the hindlimb of both species, and used to derive characteristic postures that
40 best aligned continuum-level principal stresses with cancellous bone fabric. The posture
41 identified for *Daspletosaurus* was largely upright, with a subvertical femoral orientation, whilst
42 that identified for *Troodon* was more crouched, but not to the degree observed in extant birds. In
43 addition to providing new insight on posture and limb articulation, this study also tested previous
44 hypotheses of limb bone loading mechanics and muscular control strategies in non-avian
45 theropods, and how these aspects evolved on the line to birds. The results support the hypothesis
46 that an upright femoral posture is correlated with bending-dominant bone loading and abduction-
47 based muscular support of the hip, whereas a crouched femoral posture is correlated with torsion-
48 dominant bone loading and long-axis rotation-based muscular support. Moreover, the results of
49 this study also support the inference that hindlimb posture, bone loading mechanics and muscular
50 support strategies evolved in a gradual fashion along the line to extant birds.

51

52

53

54

55

56

57

58

59

60

61 **III.2 Introduction**

62

63 The non-avian theropod dinosaurs include some of the most recognisable of extinct animals, and
64 owing to such factors as the carnivorous lifestyle and large body size of many species, they have
65 received much attention concerning various aspects of their palaeobiology (e.g., Alexander 1989;
66 Bakker 1986; Brusatte et al. 2010; Horner & Lessem 1993; Molnar & Farlow 1990). Locomotion
67 in particular is a well-studied (and sometimes controversial) topic, not only because of the
68 interest in how a giant, bipedal predator may have functioned, but also because it was likely
69 intimately tied to the evolution of the living descendants of non-avian dinosaurs, the volant birds
70 (Allen et al. 2013; Gatesy 1990; Gatesy 1995; Gatesy 2002; Gatesy & Middleton 1997;
71 Hutchinson & Allen 2009). A variety of different approaches and lines of evidence have been
72 previously used to address questions of locomotor biomechanics in non-avian theropods and its
73 evolution on the line to birds, including fossil footprints (Farlow et al. 2012; Gatesy et al. 1999;
74 Thulborn 1990), external bone shapes and proportions (Carrano 1998; Carrano 2000; Gatesy &
75 Middleton 1997; Paul 1998), bone scaling (Carrano 2001; Christiansen 1999; Gatesy 1991),
76 midshaft cortical geometry (Alexander 1989; Christiansen 1998; Farlow et al. 1995) and muscle
77 attachments and significance (Carrano & Hutchinson 2002; Gatesy 1990; Hutchinson 2001a;
78 Hutchinson 2001b). These have been more recently supplemented with various computational
79 biomechanical models, that have examined aspects such as speed capabilities (Gatesy et al. 2009;
80 Hutchinson 2004; Hutchinson & Garcia 2002; Sellers & Manning 2007), muscle moment arms
81 (Bates & Schachner 2012; Bates et al. 2012; Hutchinson et al. 2005; Hutchinson et al. 2008) and
82 mass properties (Allen et al. 2013; Allen et al. 2009; Bates et al. 2012; Bates et al. 2009a; Bates
83 et al. 2009b; Henderson 1999; Henderson & Snively 2003; Hutchinson et al. 2007)

84

85 The collective result of this prolonged and intensive research focus has been a much refined
86 understanding of how anatomy influenced non-avian theropod stance and gait, and how these
87 may have evolved on the line to extant birds. For instance, most non-avian species are inferred to
88 have used a largely upright hindlimb posture during normal locomotion, where the hips and knees
89 were flexed only to a minor degree; however, more crownward clades (e.g., paravians) may have
90 used a more crouched posture with greater flexion at the hip and knee (Hutchinson & Allen

91 2009). These postural changes are inferred to have occurred in association with changes in other
92 biomechanically important aspects, including an anterior shift in the location of the whole-body
93 centre of mass (COM; Allen et al. 2013), the muscular mechanisms of limb support and
94 propulsion (Gatesy 1990; Gatesy 1995; Gatesy 2002; Hutchinson & Gatesy 2000) and bone
95 loading mechanics (Carrano 1998). Yet, despite the important advances in understanding made,
96 there is still potential for further advances to be made, from investigation of hitherto unstudied
97 lines of evidence. One such line of evidence is the architecture of cancellous bone, which is well
98 known from studies of extant animals to be highly sensitive and well adapted to its prevailing
99 mechanical environment (cf. Part I of this series; Bishop et al. in review-c). Study of cancellous
100 bone architectural patterns in non-avian theropods may therefore provide new and unique insight
101 into various aspects of non-avian theropod locomotor biomechanics.

102

103 In Part I of this series, stark differences in hindlimb cancellous bone architecture were found
104 between humans and birds, the only obligate bipeds alive today. Many of these differences can be
105 associated with differences in the manner of striding, parasagittal, bipedal locomotion employed
106 by the two groups. In particular, the differences in cancellous bone architecture reflect differences
107 in their upright *versus* crouched postures and subsequent whole-bone loading mechanics, that is,
108 the prominence of bending and torsion. The different postures employed by humans and birds are
109 also associated with the mechanism of muscular control required to achieve limb support during
110 locomotion. In humans, mediolateral collapse of the stance phase limb is counteracted by hip
111 abduction, conferred predominantly by the gluteal muscles located dorsal to the hip (Pauwels
112 1980; Wall-Scheffler et al. 2010). However, in birds, anatomical, kinematic and
113 electromyographic evidence suggests that stance limb collapse is counteracted predominantly by
114 medial (internal) long-axis rotation of the subhorizontally oriented femur, conferred by the
115 iliopsoas muscles located anterior to the hip (Gatesy 1999b; Hutchinson & Gatesy 2000).
116 But what of extinct obligate bipeds, such as non-avian theropod dinosaurs?

117

118 In more plesiomorphic species of non-avian theropod, the architecture of cancellous bone in the
119 main hindlimb bones exhibits much similarity to that of humans, in terms of both principal fabric
120 directions in the hip and knee and whole-bone architectural patterns. In more phylogenetically
121 derived species, however, cancellous bone architecture tended to be more similar to that observed

122 in extant birds (Part I; Bishop et al. in review-c). Given that cancellous bone architectures in
123 extant obligate bipeds appear to be linked to their different locomotor biomechanics, these
124 observations raise the following questions regarding non-avian theropods:

- 125 1. Did the different species of non-avian theropods employ different limb postures?
- 126 2. Did the bones of the different species of non-avian theropods experience different loading
127 regimes?
- 128 3. Did the different species of non-avian theropods employ different strategies of muscular
129 support in counteracting stance limb collapse?
- 130 4. If the different species of non-avian theropods did employ different suites of hindlimb
131 locomotor biomechanics, how did these evolve on the line to extant birds?

132 Previously, the integration of anatomical, kinematic, bone strain and electromyographic data in
133 extant species led Carrano (1998) and Hutchinson & Gatesy (2000) to hypothesize that the
134 aforementioned aspects of bipedal locomotor biomechanics were intimately tied throughout
135 theropod evolution. The incremental change of external osteological features throughout theropod
136 evolution was also taken to indicate that the transformation in these particular biomechanical
137 aspects was a gradual occurrence (Hutchinson 2001a; Hutchinson 2001b; Hutchinson & Gatesy
138 2000). More broadly however, the exact nature of theropod locomotor evolution, in terms of
139 whether it was long and gradual, or more punctuated at certain instances, remains to be fully
140 discerned (Allen et al. 2013; Hutchinson & Allen 2009).

141

142 A new approach that can quantitatively address the aforementioned questions was outlined in Part
143 II of this series (Bishop et al. in review-b). In this ‘reverse trajectorial approach’, the observed
144 three-dimensional (3-D) architecture of cancellous bone in the main bones of the hindlimb is
145 coupled with musculoskeletal and finite element models of the hindlimb. Under a quasi-static
146 situation, these models are used to derive a single ‘characteristic posture’, one in which
147 continuum-level principal stresses best align with cancellous bone fabric. This characteristic
148 posture is a time- and load-averaged posture across all loading regimes, and it is important to
149 recognize that it may or may not be an actual posture used at a particular instance in a particular
150 behaviour.

151

152 In Part II it was shown that when applied to an extant theropod (chicken, *Gallus gallus*), the new
153 approach was able to retrieve a posture that was quite comparable to that used by birds at around
154 the midstance of normal terrestrial locomotion. It could also provide a reasonable assessment of
155 bone loading in the proximal limb (i.e., femur, proximal tibia and proximal fibula) and muscle
156 control strategies for limb stabilization, although it had markedly lower accuracy in terms of bone
157 loading in the distal limb (tibial shaft and below) and muscle control strategies for limb
158 propulsion. Additionally, it was shown that the results of this approach were largely insensitive to
159 actual muscle size (manifest as force-generating capacity), a key unknown for extinct species.
160 When applied to extinct, non-avian theropods, the approach may therefore be used to investigate
161 posture, bone loading mechanics and muscle recruitment patterns in these species as well. Thus,
162 in this approach the architecture of cancellous bone constitutes an independent data set against
163 which one or more biomechanical hypotheses may be tested.

164

165 The present study aimed to quantitatively test the hypotheses of Carrano (1998) and Hutchinson
166 & Gatesy (2000) concerning the evolution of theropod locomotor mechanics. To do this, it
167 applied the reverse trajectorial approach to two species of non-avian theropod, the basal
168 coelurosaur *Daspletosaurus torosus* and the derived paravian *Troodon formosus* (cf. Fig. 8 of
169 Part I), to derive a single characteristic hindlimb posture that best reflects these species'
170 architectural patterns of cancellous bone. These species show markedly different cancellous bone
171 architectures, with that of the former more similar to that of humans and that of the latter bearing
172 stronger resemblance to that of birds (Part I). Understanding limb posture in these and other non-
173 avian theropod species is in and of itself important, but it is also important for understanding
174 other aspects of locomotion. For instance, posture can influence maximum speed capability in
175 bipeds (Gatesy et al. 2009; Hutchinson 2004; Hutchinson & Allen 2009). In concert with the
176 results already derived from for an extant bird, the chicken (Part II), the results of this study will
177 also facilitate an examination of how locomotor biomechanics has evolved in theropods on the
178 line to extant birds.

179

180

181 **III.3 Materials and Methods**

182

183 The methodology employed in the present study followed that outlined previously in Part II
184 (Bishop et al. in review-b). Essentially, musculoskeletal models of the hindlimb in a static posture
185 were used to provide the force and boundary conditions for finite element modelling of the
186 individual limb bones, from which principal stress trajectories were determined and compared to
187 cancellous bone architectural patterns. Only those differences associated with the modelling of
188 the two different species will be described in the present study. Also, as with the previous study,
189 all assumptions and model parameters were kept in their ‘best guess’ manifestation throughout
190 the analyses; thus, differences in model results directly reflected differences in limb postures in
191 the extinct species.

192

193

194 ***III.3.1 Skeletal geometry acquisition***

195

196 The models developed in this study were derived through a combination of X-ray computed
197 tomographic (CT) scanning and photogrammetry of multiple fossil specimens; see **Table 1** for the
198 specimens (and institutional abbreviations) and imaging parameters used. The CT scans for each
199 specimen were segmented using the software Mimics 17.0 (Materialize NV, Belgium), via a
200 combination of manual and automatic techniques, to produce initial surface meshes of each bone.
201 For photogrammetry, digital photographs were taken with a Lumix DMC-TZ40 (Panasonic,
202 Japan) and rendered to produce 3-D meshes using the software Agisoft Photoscan 1.0.4 (Agisoft
203 LLC, Russia), RealityCapture 1.0 (Capturing Reality s.r.o., Slovakia), Meshlab 1.3.3
204 (<http://meshlab.sourceforge.net/>) and CloudCompare 2.5.4 (<http://www.cloudcompare.org/>).

205

206 To maximize rigour, the models for each species were based primarily on single focal individuals
207 that were relatively complete and well-preserved, and for which information on cancellous bone
208 architecture was previously reported (Part I). These were TMP 2001.036.0001 for
209 *Daspletosaurus* and MOR 748 for *Troodon*. At the time the research was undertaken, the
210 specimens used to produce the model for *Troodon* were believed to represent a single species,
211 *Troodon formosus*. However, recent research has indicated otherwise, and furthermore has cast
212 doubt on the validity of the name *Troodon formosus* itself (van der Reest & Currie 2017); the
213 majority of specimens used in this study therefore belong to an unnamed taxon. Nonetheless, the

214 model constructed here is still considered to be an accurate reflection of the anatomy of a large,
215 derived North American troodontid. Moreover, for the sake of simplicity in the present study, the
216 animal being modelled will herein be referred to as ‘*Troodon*’.

217

218 Some bones, or parts thereof, were missing from these focal specimens, and in these cases their
219 geometry was modelled using other specimens of the same or closely related species (Table 1).
220 This was achieved by scaling the geometries of these other specimens appropriately to fit the
221 focal specimens’ bones, accomplished using a combination of Mimics and the computer-aided
222 design software Rhinoceros 4.0 (McNeel, USA). Wholesale reconstruction was required for the
223 much of the pubis in *Daspletosaurus* and much of the ilium in ‘*Troodon*’. In *Daspletosaurus*, the
224 general shape of the pubis was evident from the focal specimen, but much of the boot, pubic
225 apron and ischiadic head were reconstructed based on comparison to other specimens that were
226 imaged (Table 1), personal observation of other specimens in the TMP and MOR collections, and
227 also the tyrannosaurid literature (e.g., Brochu 2003; Osborn 1917). In ‘*Troodon*’, the acetabulum,
228 antitrochanter and pubic and ischiadic peduncles were present in the focal specimen, but the
229 anterior and posterior iliac blades were reconstructed based on comparison to other troodontids
230 described in the literature (e.g., Gao et al. 2012; Tsuihiji et al. 2014; Xu et al. 2002). The
231 assembly of the individual elements of the pelvis was based on the geometry of individual bones,
232 but also on specimens of other tyrannosaurids or paravians where the pelvic elements were
233 preserved *in situ* and intact with the sacrum (e.g., Brochu 2003; Gao et al. 2012; Lambe 1917;
234 Norell & Makovicky 1997; Osborn 1917; Tsuihiji et al. 2014; Xu et al. 2002), as well as personal
235 observation of other specimens in the TMP and MOR collections and displays. For completeness,
236 the vertebral column was represented by a single cylinder fixed with respect to the pelvis. In
237 addition to the pelvis, the distalmost fibular shaft was also reconstructed for ‘*Troodon*’; it was
238 essentially a continuation of the preserved part of the shaft, tapering towards the end, and gently
239 curving laterally as it approaches the distal tibia (cf. Norell & Makovicky 1999; Ostrom 1969).

240

241 Some of the individual bones used in the above procedure had undergone a variable amount of
242 taphonomic distortion. However, in all cases this appeared to be brittle deformation only, in the
243 form of fracturing and rigid displacement of the fragments relative to one another. In these
244 instances, the bones were retro-deformed in Rhinoceros, under the assumption of brittle

245 deformation (Lautenschlager 2016). This rigid retro-deformation restored the fossil geometry
246 closer to the original geometry by realigning fragments along apposing fracture surfaces, and also
247 taking into consideration the geometry of the bones in other specimens and other species,
248 including comparison to the literature (e.g., Brochu 2003; Tsuihiji et al. 2014). The retro-
249 deformed geometries were then ‘smoothed over’ in Mimics and 3-Matic 9.0 (Materialize NV,
250 Belgium). Additionally, cracks or abraded edges were filled in and reconstructed in Mimics; only
251 the minimal amount of filling in required was undertaken.

252

253 Once an initial surface mesh had been produced for the complete geometry of each bone for both
254 species, these were smoothed in 3-matic and then refined to produce a more isoparametric mesh
255 in ReMESH 2.1 (Attene & Falcidieno 2006; <http://remesh.sourceforge.net/>). Although the tibia,
256 astragalus and calcaneum typically remain as separate ossifications in tyrannosaurids, and the
257 tibia remains separate from the astragalus and calcaneum in troodontids, the meshes of the three
258 bones were fused together in this study to create a single tibiotarsus geometry. This was
259 undertaken for the sake of simplifying the models, as well as maintaining a greater degree of
260 consistency with the previously developed chicken model of Part II.

261

262

263 ***III.3.2 Musculoskeletal modelling***

264

265 Musculoskeletal models of the right hindlimb of *Daspletosaurus* and ‘*Troodon*’ were constructed
266 in NMSBuilder (Martelli et al. 2011; Valente et al. 2014) for use in OpenSim 3.0.1 (Delp et al.
267 2007), and are shown in **Figs 1 and 2**. Both comprised 12 degrees of freedom, as in the chicken
268 model of Part II, and 38 musculotendon actuators.

269

270

271 III.3.2.1 Definition of joints

272

273 Joint locations and orientations were defined in a similar fashion to the chicken model. However,
274 the location of the hip joint was left open-ended, so as to investigate the effects of different hip
275 articulations (see Section III.3.4 below). Initially, the centre of the joint in the femur was

276 determined by fitting a sphere to the femoral head in 3-matic, and the centre of the joint in the
277 acetabulum was determined by positioning the centre of femoral head sphere in the centre of the
278 acetabulum (in both lateral and anterior views). Hence, in this initial configuration, the
279 articulation of the femur with the acetabulum was consistent with the configuration used for the
280 chicken model. It was also consistent with the inference drawn in Part I from observations of
281 cancellous bone architecture (Section I.5.2.3), that the articulation was possibly centred about the
282 apex of the femoral head. The articulation of the tibia and fibula was guided by the relative
283 positions of the fibular crest on the tibiotarsus and the flared anteromedial process of the
284 proximal fibula, as well as the facet formed distally by the tibia, astragalus and calcaneum for
285 reception of the fibula. As with the chicken model, the pes was modelled as a rectangular prism,
286 with a width set to the mediolateral width of the distal tarsometatarsus and a length set to the total
287 length of digit III; the total length of digit III for the ‘*Troodon*’ model was based on the data of
288 Russell (1969) for *Latenivenatrix mcmastrae*, scaled to the individual modelled in the current
289 study.

290

291

292 III.3.2.2 Definition of muscle and ligament anatomy

293

294 The hindlimb myology of *Daspletosaurus* and ‘*Troodon*’ was reconstructed through analysis of
295 the muscle and ligament scarring patterns observed on the fossil bones, framed in the context of
296 the myology and scarring patterns of extant archosaurs (Bates & Schachner 2012; Bates et al.
297 2012; Carrano & Hutchinson 2002; Hutchinson 2001a; Hutchinson 2001b; Hutchinson 2002;
298 Hutchinson et al. 2005; Hutchinson et al. 2008). The 33 muscles and four ligaments
299 reconstructed, along with their origins and insertions, are listed in **Table 2**. As in the chicken
300 model, the collateral ligaments of the knee and ankle were represented by four musculotendon
301 actuators in both the *Daspletosaurus* and ‘*Troodon*’ models. Each muscle was represented by a
302 single musculotendon actuator in the models, with one exception; the iliotibialis 2 (IT2) was
303 represented by two actuators on account of its probable expansive origin on the dorsal ilium
304 (Bates et al. 2012; Hutchinson et al. 2005; Hutchinson et al. 2008). The 3-D courses of the
305 actuators were constrained to follow paths that are comparable to those reported for homologous

306 muscles in extant archosaurs, and also as reconstructed for other non-avian theropod species
307 (Bates & Schachner 2012; Bates et al. 2012; Hutchinson et al. 2005; Hutchinson et al. 2008).

308

309 In reconstructing the muscular and ligamentous components of the models, a number of
310 simplifying assumptions were made. Two muscles, the ambiens (AMB) and fibularis longus (FL)
311 may possibly have sent off secondary tendons to attach more distally in the limb, as can occur in
312 extant archosaurs (Carrano & Hutchinson 2002; Hutchinson 2002). However, these secondary
313 attachments were assumed to be of little importance for bone loading mechanics as far as the
314 present study is concerned, and so were not modelled. A distal accessory tendon was considered
315 to be absent from the caudofemoralis longus (CFL), as the fourth trochanter of both species lacks
316 a distally directed process or is of small size (Carrano & Hutchinson 2002; Hutchinson 2001a). It
317 is also possible that there may have been other flexor muscles of digits II–IV in both
318 *Daspletosaurus* and ‘*Troodon*’, in addition to the flexores digitorum longus (FDL) et brevis
319 (FDB), but currently it is too speculative to infer these (Carrano & Hutchinson 2002; Hutchinson
320 2002). It was assumed in the present study that if any such digital flexor muscles were present in
321 either species, they would have had a similar disposition to the FDL, and so their action could be
322 represented by the FDL actuator.

323

324

325 III.3.2.3 Definition of segment mass properties

326

327 To estimate the mass properties of each limb segment in the *Daspletosaurus* musculoskeletal
328 model, the segment soft tissue models of Allen et al. (2013) for *Tyrannosaurus* were modified
329 appropriately to fit the pelvic and limb elements of *Daspletosaurus*. This was accomplished in
330 Rhinoceros. Likewise, the segment soft tissue models of Allen et al. (2013) for *Velociraptor* were
331 modified appropriately to fit the pelvic and limb elements of ‘*Troodon*’ in the estimation of mass
332 properties in its model. The application of the soft tissue models developed for other species to
333 the species studied here is justified, due to close phylogenetic relationship and much similarity in
334 the underlying skeletal structure between the species involved. Assuming a bulk density of 1000
335 kg/m³ for all body segments, the total mass of the right hindlimb in the *Daspletosaurus* model
336 was calculated to be 342.7 kg, and that in the ‘*Troodon*’ model was 5.65 kg.

337

338 To completely define the musculoskeletal model, this also required the calculation of mass
339 properties for the remainder of the body, that is, the pelvis segment of the models. Based on
340 femoral mid-shaft circumferences, equation 7 of Campione et al. (2014) was used to estimate the
341 total body mass for the two models. This resulted in a mass of 2757 kg for the *Daspletosaurus*
342 model and 48.5 kg for the ‘*Troodon*’ model, and hence the mass of the pelvis segment in the two
343 models (including the mass of the left hindlimb) was 2414.3 kg and 42.85 kg, respectively. By
344 unintended coincidence, in both models the mass of the right hindlimb constituted approximately
345 12% of total body weight, which therefore increased consistency between two models. For
346 comparison, the mass of the hindlimb in the chicken model of Part II constituted approximately
347 10% of total body weight. Given the data reported by Allen et al. (2013), the combined COM of
348 the whole body, minus the right leg, in their ‘average’ model of *Tyrannosaurus* was 0.544 m
349 anterior to the hip joint. The femur length of the specimen upon which their model was based is
350 1.265 m, as reported by Hutchinson et al. (2011). Scaling isometrically to the *Daspletosaurus*
351 model, which has a femur length of 0.984 m, the COM of the pelvis segment was set at 0.423 m
352 anterior to the hip. Similarly, the combined COM of the whole body, minus the right leg, in the
353 ‘average’ *Velociraptor* model of Allen et al. (2013) was 0.090 m anterior to the hip joint, and the
354 femur length upon which their model was based is 0.163 m. Thus, scaling isometrically to the
355 ‘*Troodon*’ model, which has a femur length of 0.304 m, the COM of the pelvis segment was set
356 at 0.168 m anterior to the hip. The dorsoventral position of the COM of the pelvis segment was
357 assumed to be level with the hip. As noted in Part II, the dorsoventral position of the pelvis
358 segment COM will not influence the results so long as the pelvis segment’s orientation was fixed
359 in all simulations, and all simulations were quasi-static in nature.

360

361

362 III.3.2.4 Muscle activity

363

364 Not all of the 34 musculotendon actuators representing muscles were set to be active during the
365 musculoskeletal simulations, in both *Daspletosaurus* and ‘*Troodon*’ (Table 3). The inactive
366 muscles were set using the same criteria employed for the chicken model, and through
367 comparison to published electromyography data for homologous hindlimb muscles in extant

368 archosaurs (Gatesy 1990; Gatesy 1994; Gatesy 1997; Gatesy 1999b; Jacobson & Hollyday 1982;
369 Marsh et al. 2004; Reilly & Blob 2003; Roberts et al. 1998). One exception to this was the
370 iliofemoralis externus (IFE), which in both birds and crocodylians is mostly active during the
371 swing phase of locomotion. However, in the evolutionary scenario proposed by Hutchinson &
372 Gatesy (2000), abductor muscles such as the IFE are expected to have been crucial to maintaining
373 stance limb stability, if the femur was habitually held in the subvertical orientation hypothesized
374 for most, if not all, non-avian theropods (Hutchinson & Allen 2009). Moreover, the hypothesis of
375 Hutchinson & Gatesy (2000) explains the stance phase inactivity of the IFE (or its homologues)
376 in birds and crocodylians as a result of other hip muscles conferring stance limb support, namely,
377 medial long-axis rotators in birds (iliotrochanterici) and adductors in crocodylians (adductores
378 femoris 1 et 2). Thus, to test the hypothesis of Hutchinson & Gatesy (2000), among others, the
379 IFE was set as being active in both the *Daspletosaurus* and 'Troodon' simulations. All active
380 musculotendon actuators were assigned the same maximum force capacity, equal to two times
381 body weight, that is, 54073.9 N for *Daspletosaurus* and 951.2 N for 'Troodon'.

382

383 As in the chicken simulations of Part II, a reserve actuator was applied to the
384 metatarsophalangeal joint in the musculoskeletal simulations. The maximum output of this
385 actuator in the *Daspletosaurus* and 'Troodon' simulations was scaled from that set for the
386 chicken (1,000 Nm), in proportion to the total body mass of each model: 1,767,308 Nm for
387 *Daspletosaurus* and 31,090 Nm for 'Troodon'. This corresponds to a minimum of 27 times the
388 product of body weight and total hindlimb length (sum of interarticular lengths of femur,
389 tibiotarsus and tarsometatarsus). By providing ample control of the metatarsophalangeal joint,
390 this helped reduce excessively high recruitment of the FDL and FDB.

391

392

393 III.3.2.5 Initial posture

394

395 A general mid-stance posture was used as an initial starting point, which was modified in
396 subsequent modelling iterations, as per the process outlined in Part II of this study. This initial
397 posture was based on general interpretations of tyrannosaurid and troodontid appearance in the
398 literature (technical and popular). Additionally, the hip extension angle was initially set so that

399 the knee joint was near the line of the vertical ground reaction force in the x - z (sagittal) plane,
400 following previous interpretations of theropod hindlimb biomechanics (Gatesy et al. 2009;
401 Hutchinson & Gatesy 2006).

402

403

404 ***III.3.3 Finite element modelling***

405

406 Finite element simulations of the *Daspletosaurus* and ‘*Troodon*’ models were developed and
407 solved in largely the same manner as the previously described chicken simulations of Part II,
408 using ANSYS 17.0 (Ansys, Inc., USA). Two minor differences were that (i) a graduated and finer
409 mesh was used around the cleft of the lesser trochanter of the *Daspletosaurus* femur, to reduce
410 stress artifacts, and (ii) connection between the tibiotarsus and fibula entities was modelled both
411 proximally and distally. The latter difference reflects that fact that both tyrannosaurs and
412 troodontids possessed a distinct furrow in the distal tibiotarsus for reception of the distal fibula,
413 whereas in birds the distal fibula is greatly reduced. In the *Daspletosaurus* model, the total
414 number of elements used across the various postures tested ranged from 961,023 to 975,544 in
415 the femur simulation and from 985,071 to 1,005,550 in the tibiotarsus + fibula simulation. In the
416 ‘*Troodon*’ model, the total number of elements used across the various postures tested ranged
417 from 668,033 to 684,547 in the femur simulation and from 583,228 to 598,556 in the tibiotarsus
418 + fibula simulation.

419

420

421 ***III.3.4 Varying hip articulation***

422

423 Following the identification of a ‘solution posture’ for the *Daspletosaurus* model, a brief
424 exploratory exercise was undertaken to address the ambiguity surrounding the articulation of
425 non-avian theropod hips. Unlike birds, many non-avian theropods typically possessed a large
426 incongruence in size between the femoral head and the acetabulum; for example, in the
427 *Daspletosaurus* focal specimen studied, the diameter of the femoral head is about two-thirds that
428 of the acetabulum (Fig. 3). This has consequently created uncertainty in exactly how the femur
429 articulated with the acetabulum in these extinct species. It has been previously suggested that the

430 main area of articulation on the femur occurred on the roughly cylindrical part of the femoral
431 head, lateral to the apex of the head (e.g., Hotton 1980; Hutchinson & Allen 2009). However,
432 cancellous bone architectural patterns observed in *Allosaurus* and tyrannosaurids (Part I) suggest
433 that hip joint loads may have been transmitted through the femoral head mainly from the apex of
434 the head, not from the more lateral parts.

435

436 To examine the effect of different hip articulations in the *Daspletosaurus* model, this was varied
437 to assess if any improvement in correspondence between principal stress trajectories and
438 cancellous bone architecture was possible beyond that of the solution posture (Fig. 3). Two such
439 variations were made. Firstly, the femur was moved 50 mm medially with respect to the
440 acetabulum, so that a sizeable proportion of the cylindrical part of the femoral head was in close
441 proximity to the acetabulum (Fig. 3C,D). The rest of the limb was also moved medially along
442 with the femur, including the coordinate systems of distal joints and all musculotendon actuator
443 origins, insertions and via points that were level with or distal to the hip. So as to maintain a
444 similar mediolateral foot placement as the original solution posture, the amount of hip abduction-
445 adduction was altered slightly. In the second variation, the femur and limb distal to it was again
446 moved 50 mm medially with respect to the acetabulum, but the hip was also abducted by 14°,
447 producing a net 10° abduction from the neutral posture (Fig. 3E,F). This reflects the amount of
448 hip abduction that has been supposed for tyrannosaurids in previous modelling studies (e.g.,
449 Hutchinson et al., 2005, 2007), on account of the inclined disposition of the femoral head relative
450 to the long-axis of the femur. In order to bring the foot anywhere near the body midline, this
451 abducted posture also necessitated a large 27° of external long-axis rotation of the hip, a value
452 comparable to maximal external long-axis rotation in modern birds during straight-line
453 locomotion (Kambic et al. 2015; Rubenson et al. 2007).

454

455

456 *III.3.5 Cross-species patterns*

457

458 Once solution postures were identified for both the *Daspletosaurus* and ‘*Troodon*’ models, a
459 number of biomechanically relevant parameters were extracted. The same parameters were also
460 extracted from the solution posture identified previously for the chicken model of Part II. By way

461 of comparison across the three species, these parameters would allow a quantitative assessment
 462 of the evolutionary-biomechanical hypotheses of Carrano (1998) and Hutchinson & Gatesy
 463 (2000). Three sets of parameters were extracted:

- 464 1. *Postural parameters*, related to Question 1 posed in the Introduction: the location of the
 465 whole-body COM as normalized by total hindlimb length, joint angles for the hip and knee,
 466 and the ‘degree of crouch’, both actual and predicted from empirical data reported by Bishop
 467 et al. (in review-a).
- 468 2. *Bone loading parameters*, related to Question 2 posed in the Introduction: the orientation of
 469 principal stresses at the femoral mid-shaft, the ratio of maximum shear stress to bending
 470 stresses at the femoral mid-shaft, and the orientation of the neutral axis of bending at the
 471 femoral mid-shaft, relative to the mediolateral axis. To enable estimation of these parameters
 472 at mid-shaft, a local long-axis in the vicinity of the mid-point of the bone was determined.
 473 This was calculated by fitting a cylinder to the shaft in the immediate vicinity of the mid-
 474 point, calculated in 3-matic; the long-axis of the cylinder defined the local long-axis of the
 475 bone, and the plane normal to this axis defined the plane of the mid-shaft cross-section. The
 476 orientation of principal stresses was defined as the orientation of the steepest inclined stress
 477 vector with respect to the local long-axis; this was calculated separately for both σ_1 and σ_3 ,
 478 and then the mean orientation was taken. In pure bending the orientation would be 0° , that is,
 479 parallel to the long-axis, and in pure torsion it would be 45° (Beer et al. 2012). Additionally,
 480 mid-shaft bending stresses were calculated as

$$481 \quad \sigma_{\text{bending}} = \frac{|\sigma_{\text{max}}| + |\sigma_{\text{min}}|}{2}, \quad (1)$$

482 where σ_{max} is the maximum (tensile) stress at mid-shaft and σ_{min} is the minimum
 483 (compressive) stress at mid-shaft. This assumes that planar strain conditions were in place
 484 (Biewener 1992), which was revealed by inspection of normal stress contours to be
 485 approximately true.

- 486 3. *Muscular support parameters*, related to Question 3 posed in the Introduction: the abduction
 487 moments of muscles that are predominantly suited to conferring hip abduction (i.e.,
 488 iliofemoralis externus), and the long-axis rotation moments of muscles that are
 489 predominantly suited to conferring hip long-axis rotation (i.e., iliotrochantericus caudalis and
 490 puboischiofemorales internus 1 et 2 in non-avian theropods; iliotrochanterici caudalis et

491 medialis in the chicken). By being normalized to the product of the model's body weight and
 492 hip height, these moments give a size-independent measure of how much 'effort' a muscle
 493 exerts to stabilize a joint in a given axis:

$$494 \quad M^* = \frac{a \cdot F_{\max} \cdot r_i}{m \cdot g \cdot h}, \quad (2)$$

495 where a is the activation level of the muscle, from 0 (inactive) to 1 (maximally active), F_{\max}
 496 is the maximum force capable of being produced (set at two body weights as per Part II), r_i is
 497 the muscle's moment arm about joint axis i , m is body mass, g is the acceleration due to
 498 gravity (9.81 m/s^2) and h is hip height. It is worth noting that this analysis carries the caveat
 499 of ignoring biarticular muscles (e.g., iliotibiales) and co-contraction between agonistic and
 500 antagonistic muscles.

501

502 Given the small sample size of species examined here ($n = 3$), any assessment of the evolution of
 503 biomechanically relevant parameters is necessary a coarse one. Since the hindlimb anatomy of
 504 *Daspletosaurus* is close to that inferred for the ancestral state of Coelurosauria, its results may
 505 taken to be representative of the most recent common ancestor of it and 'Troodon'; likewise,
 506 since the anatomy of the 'Troodon' model is close to that inferred for the ancestral state of
 507 Paraves, its results may taken to be representative of the most recent common ancestor of it and
 508 the chicken. Thus, by mapping results towards the most recent common ancestor of successive
 509 clades, the changes observed between *Daspletosaurus*, 'Troodon' and the chicken are taken to be
 510 a surrogate for the actual sequence (if not pattern) of evolution along the theropod stem lineage.

511

512

513 **III.4 Results**

514

515 A total of five different postures for *Daspletosaurus*, and six postures for 'Troodon', were tested
 516 before no further correspondence between principal stress trajectories and cancellous bone
 517 architectural patterns was able to be achieved (Fig. 4A,B). In the *Daspletosaurus* model, going
 518 from the worst to best postures tested, the angular deviation between the minimum compressive
 519 stress (σ_3) and the mean direction of the primary fabric orientation (\mathbf{u}_1) in the femoral head
 520 decreased from 15.6° to 7.3° , a 53% reduction; likewise, the angular deviation between σ_3 and \mathbf{u}_1

521 in the medial femoral condyle decreased from 11.7° to 2.8° , a 76% reduction. In the ‘*Troodon*’
522 model, going from the worst to best postures tested, the angular deviation between σ_3 and u_1 in
523 the femoral head decreased from 23.8° to 3.9° , an 84% reduction; likewise, the angular deviation
524 between σ_3 and u_1 in the medial femoral condyle decreased from 28.3° to 24.2° , a 14% reduction.
525 The final solution postures for both species are illustrated in Fig. 4C–H. As with the results for
526 the chicken model (Part II), only minimal correspondence between principal stress trajectories
527 and cancellous bone architecture was able to be achieved in the distal tibiotarsus of either species.
528 Little correspondence was also able to be achieved in the fibular crest of the *Daspletosaurus*
529 model’s tibia. Thus, the remainder of this section will focus on the more proximal parts of the
530 hindlimb.

531

532

533 *III.4.1 Daspletosaurus results*

534

535 In the solution posture, the principal stress trajectories in the femur showed a high degree of
536 correspondence with the observed cancellous bone architecture throughout the bone (Figs 4A, 5,
537 6). Strong correspondence between σ_3 (compressive) and cancellous bone architecture occurred
538 in the femoral head and both medial and lateral femoral condyles. This correspondence included
539 that between the mean direction of σ_3 and u_1 (Figs 5G, 6I). Correspondence between the
540 maximum principal stress (σ_1 , tensile) and cancellous bone architecture occurred in the distal half
541 of the fourth trochanter. Additionally, three instances of a double-arcuate pattern occurred,
542 formed by σ_1 and σ_3 , largely in the coronal plane. These correlate to three similar such patterns
543 observed in the cancellous bone architecture of tyrannosaurids: in the femoral head and proximal
544 metaphysis, in the lesser trochanter, and in the anterior and posterior parts of the distal femur
545 proximal to the condyles. The double-arcuate patterns of σ_1 and σ_3 sometimes also occurred in
546 the results for other postures tested, but they were often less developed compared to the solution
547 posture.

548

549 Strong correspondence between principal stress trajectories and cancellous bone architecture also
550 occurred in the proximal tibia and fibula (Fig. 7). The trajectory of σ_3 corresponded closely with
551 the observed architectural patterns of both the medial and lateral condyles, including a more

552 lateral inclination in the lateral condyle. In the cnemial crest of the tibia, the trajectory of σ_1
553 largely paralleled the margins of the crest, as observed for cancellous bone fabric. Good
554 correspondence between σ_3 and cancellous bone architectural patterns was also observed in the
555 fibular head, particularly for in the medial aspect of the bone (Fig. 7K,L).

556

557

558 **III.4.2 ‘Troodon’ results**

559

560 As with the *Daspletosaurus* model, in the solution posture identified for ‘*Troodon*’, the principal
561 stress trajectories in the femur generally showed strong correspondence to the observed
562 cancellous bone architecture (Figs 4B, 8, 9). Correspondence with σ_3 occurred in the femoral
563 head, under the greater trochanter and in both medial and lateral condyles; correspondence with
564 σ_1 occurred in the lesser trochanter. The mean direction of σ_3 in the femoral head showed strong
565 correspondence to the mean direction of \mathbf{u}_1 (Fig. 8E). A decent amount of correspondence
566 between σ_3 and \mathbf{u}_1 also occurred in the medial femoral condyle, although the direction of σ_3 was
567 notably more posteriorly inclined than the mean direction of \mathbf{u}_1 (Fig. 9E), as occurred in the
568 chicken model of Part II. Unlike the results for the *Daspletosaurus* model, no double-arcuate
569 pattern of σ_1 and σ_3 was present in ‘*Troodon*’; instead, their trajectories tended to spiral about the
570 bone’s long axis, much like the stress results for the chicken model.

571

572 Good correspondence between principal stress trajectories and cancellous bone architecture also
573 occurred in the proximal tibia and fibula (Fig. 10). In the medial and lateral condyles, σ_3
574 corresponded closely with observed architectural patterns, possessing a gentle posterior
575 inclination, with a slight lateral inclination under the lateral condyle. In the cnemial crest, the
576 trajectory of σ_1 largely paralleled the margins of the distal part of the crest. In the fibular head,
577 the principal stress trajectories showed good overall correspondence to the observed architectural
578 patterns (Fig. 10K–M). Greater correspondence occurred laterally with σ_1 , but some
579 correspondence was also present in the medial side with σ_3 .

580

581

582 **III.4.3 Hip articulation results**

583

584 In both variations in hip articulation tested for the *Daspletosaurus* model, the resulting principal
585 stress trajectories of the proximal femur showed poorer correspondence with observed cancellous
586 bone architecture than that achieved with the initial solution posture (Fig. 11). In particular, σ_3 ,
587 was broadly directed towards the more cylindrical part of the femoral head, lateral to the apex,
588 rather than towards the apex itself. Additionally, the anterior inclination of σ_3 in the femoral head
589 was greater in both variations than that in the originally identified solution posture, and was
590 markedly greater than the anterior inclination of the mean direction of \mathbf{u}_1 .

591

592

593 *III.4.4 Cross-species comparisons of biomechanical parameters*

594

595 In terms of posture, hip extension, hip adduction-abduction, hip long-axis rotation and knee
596 flexion angles all changed in a gradual fashion progressing from *Daspletosaurus* to ‘*Troodon*’ to
597 the chicken (Fig. 12). The same pattern also occurred for the anterior location of the whole-body
598 COM and the degree of crouch. Furthermore, the degree of crouch of the solution postures
599 matched closely with empirical predictions based on total leg length (Fig. 12C). In terms of bone
600 loading, all parameters also changed in a gradual fashion progressing from *Daspletosaurus* to the
601 chicken (Fig. 13A,B). Thus, in *Daspletosaurus*, the femur was loaded predominantly in
602 mediolateral bending, whereas in the chicken the femur was loaded predominantly in torsion,
603 with bending predominantly of an anteroposterior nature. In ‘*Troodon*’, torsion was more
604 prominent compared to *Daspletosaurus*, but bending still remained the dominant loading regime.
605 As with the other parameters, muscular support also changed gradually progressing from
606 *Daspletosaurus* to the chicken (Fig. 13C,D). In *Daspletosaurus*, the normalized hip abductor
607 moment was relatively high and the normalized hip medial rotator moment was relatively low,
608 whereas the situation was reversed in the chicken.

609

610

611 **III.5 Discussion**

612

613 Having previously demonstrated the validity and potential utility of the ‘reverse’ application of
614 the trajectorial theory (Part II; Bishop et al. in review-b), the aim of the present study was to
615 apply this approach to two extinct, non-avian theropods, *Daspletosaurus torosus* and ‘*Troodon*’
616 (*Troodontidae* sp.), to gain new insight into their hindlimb locomotor biomechanics. In addition
617 to deriving a ‘characteristic posture’ for both species, quantitative results were produced that
618 have bearing on various questions concerning theropod locomotor biomechanics and its
619 evolution, posed in Section III.2. In particular, the evolutionary-biomechanical hypotheses of
620 Carrano (1998) and Hutchinson & Gatesy (2000) were able to be quantitatively tested in a novel
621 way.

622

623

624 ***III.5.1 Postures***

625

626 In the ‘characteristic posture’ identified for both non-avian theropods, there was generally a
627 strong alignment between calculated principal stress trajectories and observed patterns in
628 cancellous bone architecture, across the femur, proximal tibia and proximal fibula. It is important
629 to note that this should not be presumed to be *the* posture used by these extinct species at any
630 particular point in the stance phase; rather, the posture identified here is a time- and load-
631 averaged characterization of the kinds of postures experienced on a daily basis. Nevertheless,
632 since the posture previously identified for the chicken corresponds well to the posture of a typical
633 avian hindlimb at around mid-stance in terrestrial locomotion (Part II), the postures derived for
634 *Daspletosaurus* and ‘*Troodon*’ are inferred to reflect the postures of these species at around the
635 mid-stance of normal locomotion. Thus, *Daspletosaurus* is inferred to have stood and moved
636 with a largely upright posture with a subvertical femoral orientation, whilst the limb posture of
637 ‘*Troodon*’ is inferred to have been more crouched, although not to the degree observed in extant
638 birds. It is worth noting that the femoral orientation of the *Daspletosaurus* posture, in terms of the
639 degree of hip extension, is very similar to that hypothesized for other large, basal tetanuran
640 species by previous workers such as *Tyrannosaurus* (Gatesy et al. 2009; Hutchinson 2004;
641 Hutchinson et al. 2005), *Allosaurus* and *Acrocanthosaurus* (Bates et al. 2012). The inferences
642 drawn in those studies were based on the posture that allowed for high locomotor forces to be
643 sustained (Gatesy et al. 2009; Hutchinson 2004), or that achieved a maximal total moment arm of

644 the hip extensor muscles (Bates et al. 2012; Hutchinson et al. 2005). The rationale of the latter set
645 of studies is in some respects similar to the approach of the present study (which used static
646 optimization in the musculoskeletal modelling stage), in that both approaches are dependent on
647 the moment arms of individual muscles (see Part II, section II.5.1).

648

649

650 ***III.5.2 Articulation of the non-avian theropod hip joint***

651

652 The results of the exploratory analysis of hip articulations in the *Daspletosaurus* model supported
653 the inference made in Part I of this series: in non-avian theropods such as *Allosaurus* and
654 tyrannosaurids, the immediate articulation between the femur and acetabulum may have been
655 centred about the apex of the femoral head. Other articulations, involving greater contribution
656 from the cylindrical part of the femoral head lateral to the apex, did not result in as strong
657 correspondence between principal stresses and cancellous bone architecture. This is not to say
658 that these other articulations were not used during daily activity, rather that they may have been
659 used less frequently. Indeed, as the entire proximal surface of the non-avian theropod femur
660 typically bears a smooth, wrinkled texture indicative of a hyaline cartilage covering (Tsai &
661 Holliday 2015), this suggests that articulation between the lateral proximal femur and the
662 incipient antitrochanter on the ilium would have occurred on occasion, but the relatively
663 frequency of this remains unknown (see also Kambic et al. 2014; Kambic et al. 2015). This
664 interpretation of hip articulation is also consonant with anatomical considerations of the non-
665 avian theropod pelvis and sacrum. Specifically, a more lateral articulation of the (non-abducted)
666 femur with the acetabulum places the femoral head more medially with respect to the pelvis,
667 which could bring it into contact with the centra of the sacral vertebrae (e.g., Gilmore 1920;
668 Osborn 1917; Rauhut & Carrano 2016).

669

670 Combined with the results of the exploratory analysis, the solution posture identified for the
671 *Daspletosaurus* model can help move toward resolving the question of how theropods with
672 proximomedially inclined femoral heads, such as tyrannosaurids and carcharodontosaurids, kept
673 their feet positioned close to the body midline, as indicated by fossil trackways (e.g., McCrea et
674 al. 2014). Previously, working on the assumption that the cylindrical part of the femoral head

675 articulated with the acetabulum, researchers had found that the femur inevitably becomes
676 markedly abducted from the body midline. Without further speculation about joint articulations
677 or the nature of the intervening soft tissues (cartilage, menisci) more distally in the limb, this
678 leads to an unnaturally wide foot placement (e.g., Bates et al. 2012; Hutchinson et al. 2005;
679 Hutchinson et al. 2007). Indeed, in the second variation of hip articulation tested for the
680 *Daspletosaurus* model, mediolateral step width was almost 47% of hip height, more than three
681 times the typical step width observed in theropods (Bishop et al. 2017). With the hip articulation
682 occurring at the apex of the femoral head, however, this allows for significant joint movement in
683 other directions besides abduction-adduction. In particular, the solution posture identified for the
684 *Daspletosaurus* model had a modest amount of external long-axis rotation, but little abduction of
685 the femur; in fact, the femur was adducted slightly. Moreover, the asymmetry of the distal
686 femoral condyles leads to a gently skewed orientation of the knee flexion-extension axis in the
687 coronal plane, such that the distal crus is angled in towards the body midline (see Part II and **Figs**
688 **1E and 2E**). The combination of these features allows the pes to be positioned close to the
689 midline, yet the upper limb be kept clear of the pelvis.

690

691 Despite the potential that this new interpretation may have for understanding how non-avian
692 theropod hips may have articulated, it is worth emphasizing that it is based on a single posture,
693 which at best can only be regarded as a snap shot of the limb during the stance phase of
694 locomotion. A great deal more work is required if an understanding of dynamic joint articulations
695 throughout the stride is to be achieved. One potential avenue is by using forward dynamic
696 simulations (e.g., Sellers et al. 2017) to generate a variety of postures throughout the stance that
697 may be used to inform musculoskeletal and finite element models. This would require more
698 complex modelling of some joints than is currently done (e.g., three degrees of freedom for the
699 hip), and would in turn require substantially greater computational power.

700

701

702 ***III.5.3 Theropod locomotor evolution***

703

704 A second major objective of the current study was to test evolutionary-biomechanical hypotheses
705 concerning posture, bone loading mechanics and muscular control strategies in theropods. In

706 doing so, insight would be gained as to how such aspects of theropod locomotion may have
707 evolved on the line to birds. The results for the three theropod species modelled here demonstrate
708 that, progressing through theropod phylogeny towards more derived species, the following trends
709 occurred:

- 710 1. The whole-body COM moved anteriorly; this was to be expected, given that model mass
711 properties were largely derived from models developed in the study of Allen et al. (2013),
712 who showed the same pattern.
- 713 2. Hindlimb posture became more crouched, at least as far as the hip and knee joints are
714 concerned. This is consonant with the findings of previous work (Carrano 1998; Gatesy
715 1990; Gatesy 1991).
- 716 3. Torsion became more prevalent than bending as the dominant loading regime of the femur.
- 717 4. The direction of bending of the femur changed from being predominantly mediolateral to
718 being predominantly anteroposterior.
- 719 5. Hip abduction became overtaken by hip long-axis rotation as the main muscular control
720 mechanism of stance-limb support.

721 For a given parameter, the value for '*Troodon*' was intermediate between that for *Daspletosaurus*
722 and that for the chicken. This supports the hypothesis of a gradual evolutionary change in
723 locomotor biomechanics along the line to birds, but more taxa from different parts of theropod
724 phylogeny would need to be modelled to definitively rule out punctuated change at any point
725 along the stem lineage. Regardless of the mode of evolution of these parameters, the above
726 results do suggest that hindlimb posture, bone loading mechanics and muscular support strategies
727 were tightly associated with each other, supporting the hypotheses of Carrano (1998) and
728 Hutchinson & Gatesy (2000). Future development of models for other non-avian theropod
729 species will help further test this interpretation.

730

731 The above trends identified in the present study parallel trends in other biomechanically relevant
732 aspects, as noted by previous studies. These other trends include:

- 733 1. Modifications of pelvic and hindlimb osteology and musculature (Carrano 2000; Hutchinson
734 2001a; Hutchinson 2001b; Hutchinson 2002).
- 735 2. Decrease in tail length and prominence of caudofemoralis musculature (Gatesy 1990; Gatesy
736 1995; Gatesy 2002; Pittman et al. 2013).

- 737 3. A shift from caudofemoralis-mediated, hip-based limb retraction to ‘hamstring’-mediated,
738 knee-based limb retraction during gait (Gatesy 1990; Gatesy 1995; Gatesy 2002).
- 739 4. Changes in gross limb proportions, in particular a decrease in relative femur length, which in
740 turn leads to an apparent increase in femoral diaphyseal robusticity (Carrano 1998; Gatesy &
741 Middleton 1997).
- 742 5. The acquisition of a more continuous locomotor repertoire, where walking and running are
743 not discrete gaits (Bishop et al. 2017).

744 The timing of some of these changes remains uncertain (see also Hutchinson 2006), but it appears
745 that all were underway prior to the origin of Paraves (i.e., birds and their closest maniraptoran
746 relatives such as ‘*Troodon*’), and that many, if not all, took place over a protracted period of time.

747

748 Most of the above changes also occurred in tandem with a progressive (Lee et al. 2014) or multi-
749 step (Benson et al. in press) reduction in body size along the theropod stem lineage. A decrease in
750 body size – either along the theropod stem lineage, or by directly comparing *Daspletosaurus*,
751 ‘*Troodon*’ and the chicken – might be expected in and of itself to bring about changes in posture,
752 since posture correlates with body size in extant parasagittal tetrapods (Biewener 1989; Biewener
753 1990; Bishop et al. in review-a; Gatesy & Biewener 1991). However, since many other aspects of
754 theropod anatomy and locomotor biomechanics also change in tandem with body size along the
755 theropod stem lineage, it is presently not possible to disentangle the relative importance of body
756 size (or any other single feature) on posture. That many aspects of theropod locomotor anatomy
757 and biomechanics appear to have co-evolved over a protracted period of time, along with
758 additional features such as forelimb enlargement (Dececchi & Larsson 2013) and elaboration of
759 forelimb integument (Xu et al. 2014; Zelenitsky et al. 2012), is an interesting phenomenon that
760 warrants further investigation.

761

762 The results of this study may also have more general implications for understanding locomotor
763 biomechanics (and its evolution) in tetrapod species that employ a largely parasagittal stance and
764 gait. Previous *in vivo* strain gauge studies of parasagittal mammals that use a more crouched
765 femoral posture have shown that the femur experiences a sizeable amount of torsional loading, in
766 addition to bending (Butcher et al. 2011; Keller & Spengler 1989). Additionally, finite element
767 simulations of sit-to-stand and stand-to-sit behaviour in humans, behaviours that require limb

768 support during crouched femoral orientations, have revealed a marked increase in torsional
769 loading of the femur compared to normal locomotion (Villette 2016). In concert with the results
770 of this study, these observations suggest that there is a continuum in musculoskeletal mechanics
771 spanning from crouched to upright postures, of which birds and humans are ‘end members’. In
772 upright postures, hip abduction is the dominant mode of limb support, which results in bending
773 being the dominant mode of loading of the femur. However, as the femur becomes more
774 crouched, the efficacy of hip abduction in providing limb support decreases, whilst that of hip
775 long-axis rotation increases; this in turn loads the femur in a greater degree of torsion (see also
776 Butcher et al. 2011).

777

778

779 *III.5.4 Methodological considerations*

780

781 A number of methodological considerations should be borne in mind when interpreting the
782 results of the present study. None are considered to be of any major importance for the main
783 interpretations made here, but they do highlight areas where future research efforts could be
784 focused, potentially yielding further insight into theropod hindlimb biomechanics.

785

786

787 III.5.4.1 Correspondence in the distal tibiotarsus

788

789 It is worth re-iterating that little correspondence was able to be achieved between principal
790 stresses and cancellous bone architecture in the distal parts of the tibiotarsus or fibula, in any
791 posture tested for all three theropod species modelled. Additionally, the architectural patterns
792 observed in the fibular crest of tyrannosaurid tibiae could not be replicated in the *Daspletosaurus*
793 model. As discussed in Part II, this could reflect an inadequate modelling formulation, adaptation
794 of these parts of the bones to many varied loading regimes, or a combination of both (or other)
795 factors. Despite this, the architecture of cancellous bone in the distal tibiotarsus of theropods
796 shows some strikingly different patterns between the various theropod groups. From a
797 phenomenological perspective at least, this is indicative of marked differences in bone loading
798 regimes, and by extension locomotor behaviour. It is therefore worthy of future modelling effort

799 to establish a more mechanistic link between cancellous bone architecture and musculoskeletal
800 loading mechanics in this part of the hindlimb.

801

802

803 III.5.4.2 Pelvic orientation

804

805 One aspect of theropod posture that was not investigated in this study was the orientation of the
806 pelvis. In all simulations, the pelvis of the three theropod species modelled was oriented
807 similarly, with the sacral vertebra oriented approximately horizontally and parallel to the x -axis
808 of the global coordinate system. However, it is known that extant birds can employ significant
809 amounts of pitch, roll or yaw during locomotion (Abourachid et al. 2011; Gatesy 1999a;
810 Rubenson et al. 2007). If the pelvis underwent side-to-side rolling during locomotion in non-
811 avian theropods, even by a small amount, this may have served to clear the pelvis and trunk
812 further out of the way of the thigh of the stance leg. The effect of this would have been most
813 obvious in species with well-developed pubic boots, such as large tyrannosaurids and
814 allosauroids. Future investigation could therefore be directed towards incorporating one or more
815 degrees of freedom in the pelvis segment of the models, as well incorporating additional degrees
816 of freedom in other joints (e.g., knee) too. Caution would need to be exercised, however, as the
817 number of variable parameters could quickly grow to be very large, which may require a great
818 deal more iterations be tested before a ‘solution posture’ is satisfactorily obtained.

819

820

821

822

823

824 III.5.4.3 Stresses in the medial femoral condyle

825

826 As noted in the results of this study, as well as those of Part II, the mean direction of the
827 minimum principal stress (σ_3) in the medial femoral condyle was notably more posteriorly
828 inclined than the mean direction of the primary fabric orientation of cancellous bone (\mathbf{u}_1), in both
829 the chicken and ‘*Troodon*’ models. This was the case regardless of the posture tested. The cause

830 for this discrepancy is probably twofold. Firstly, taking the mean direction of \mathbf{u}_1 in the medial
831 condyle will average out the ‘fan’ of individual fabric vectors (see Part I) that is ubiquitous in
832 theropods. Thus, there will be some parts of the condyle for which a greater correspondence
833 between fabric direction and the calculated principal stresses will indeed occur, namely, where
834 the fabric vectors are more posteriorly inclined than the overall orientation.

835

836 Secondly, it is quite possible that the individual \mathbf{u}_1 vectors throughout the medial condyle may
837 also ‘reflect’ the maximum principal stress (σ_1) in addition to σ_3 , and so do not fully align with
838 the calculated directions of either one. Given that motion of the theropod knee is inferred to have
839 predominantly occurred in the flexion-extension plane (but see Kambic et al. 2015), the main
840 loading regimes expected in the femoral condyles would be expected to be anteroposteriorly
841 oriented, as also suggested by the ‘butterfly pattern’ of the secondary fabric direction in the
842 condyles (see Part I). Hence, both σ_1 and σ_3 could be expected to be largely constrained to a
843 parasagittal orientation, which could influence the direction of \mathbf{u}_1 throughout the medial condyle.

844

845

846 **III.6 Conclusion**

847

848 By applying the trajectorial theory in reverse, this study sought to identify a single, characteristic
849 posture for two extinct, non-avian theropods that can explain a considerable amount of the
850 architecture of cancellous bone observed in the hindlimb bones of these species. The postures
851 derived for *Daspletosaurus torosus* and ‘*Troodon*’ are inferred to reflect the postures used at
852 around mid-stance during normal terrestrial locomotion, but should not be presumed to have been
853 *the* postures used. The largely upright posture identified for *Daspletosaurus* is comparable to the
854 postures previously hypothesized for other large, basal tetanuran species of non-avian theropod.
855 The posture identified for ‘*Troodon*’ is more crouched than that of *Daspletosaurus*, especially in
856 regard to femoral orientation, but not to the degree observed in extant birds. The results of this
857 study also provide an alternative perspective on the manner of articulation of the non-avian
858 theropod hip joint, and suggest a solution to how non-avian theropods with proximomedially
859 inclined femoral heads maintained narrow mediolateral foot placements.

860

861 In addition to improving understanding of posture in non-avian theropods, this study provides a
862 new approach for how evolutionary-biomechanical hypotheses of locomotion can be explicitly
863 and quantitatively tested. By using a previously underexplored line of evidence, cancellous bone
864 architecture, the results of this study have supported the hypotheses of Carrano (1998) and
865 Hutchinson & Gatesy (2000). Progressing from basal tetanurans and coelurosaurs through to
866 extant birds, a number of important changes are inferred to have occurred in concert with one
867 another, involving whole-body COM position, hindlimb posture, bone loading mechanics and
868 muscular control strategies. The pattern of the changes also supports a more gradual fashion of
869 change (as opposed to more punctuated), adding to the growing body of evidence suggesting that
870 the unique locomotor repertoire of extant birds was acquired over a long period of time.
871 However, only three species were modelled here, and so a more rigorous testing of the exact
872 mode and tempo of evolutionary change awaits the modelling of additional species.

873

874 The integrative biomechanical modelling approach developed in Part II provides useful insights
875 into non-avian theropod hindlimb locomotor biomechanics, as well as how this evolved along the
876 line to extant birds. The generality of the approach means that it could be useful for
877 understanding locomotor behaviour, and its evolution, in other extinct vertebrate groups as well.
878 Examples of future research that could apply the approach include: forelimb posture and use in
879 quadrupedal dinosaurs, such as ceratopsians (Fujiwara & Hutchinson 2012; Johnson & Ostrom
880 1995); the evolution of powered flight in birds, bats and pterosaurs (Bishop 2008; Heers & Dial
881 2012; Thewissen & Babcock 1992; Unwin 2005); the evolution of posture in synapsids on the
882 line to mammals (Blob 2001; Kemp 1982); and the evolution of terrestrial locomotor capabilities
883 in stem tetrapods (Clack 2012; Pierce et al. 2013). It may also prove to be of use for questions of
884 biomechanics not related to locomotion, such as the posture of sauropod dinosaur necks (Stevens
885 & Parrish 2005; Taylor et al. 2009).

886 **III.7 Acknowledgements**

887

888 The staff of the Geosciences Program of the Queensland Museum is thanked for the provision of
889 workspace and access to literature: A. Rozefelds, K. Spring, R. Lawrence, P. Tierney, J.
890 Wilkinson and D. Lewis. Much appreciation is extended to the staff and associated colleagues of
891 the institutions that provided access to the material studied here: D. Henderson, B. Strlisky, G.

892 Housego, R. Russel, T. Courtenay, B. Sanchez and F. Therrien (Royal Tyrell Museum of
893 Palaeontology, Drumheller); R. Irmis, C. Levitt-Bussian, C. Webb and P. Policelli (Natural
894 History Museum of Utah, Salt Lake City); J. Horner, J. Scannella, D. Varricchio, D. Strosnider,
895 C. Woodruff, D. Fowler and T. Carr (Museum of the Rockies, Bozeman). Many of the above
896 people also provided helpful discussion on various aspects of theropod biology, and also helped
897 transport specimens for CT scanning. Those who facilitated or performed the scanning itself are
898 also greatly thanked: S. Purdy and D. Wetter (Canada Diagnostic Centres, Calgary); K. Ugrin and
899 D. Van Why (Bozeman Deaconess Hospital, Bozeman); and S. Merchant, E. Hsu and J. Morgan
900 (HSC Cores Research Facility, University of Utah, Salt Lake City). All scripts and data used are
901 held in the Geosciences Collection of the Queensland Museum, and will be made available upon
902 request to the Collections Manager.

903

904

905 **III.8 References**

906

- 907 Abourachid A, Hackert R, Herbin M, Libourel PA, Lambert F, Gioanni H, Provini P, Blazevic P,
908 and Hugel V. 2011. Bird terrestrial locomotion as revealed by 3-D kinematics. *Zoology*
909 114:360–368.
- 910 Alexander RM. 1989. *Dynamics of Dinosaurs and Other Extinct Giants*. New York: Columbia
911 University Press.
- 912 Allen V, Bates KT, Li Z, and Hutchinson JR. 2013. Linking the evolution of body shape and
913 locomotor biomechanics in bird-line archosaurs. *Nature* 497:104–107.
- 914 Allen V, Paxton H, and Hutchinson JR. 2009. Variation in Center of Mass Estimates for Extant
915 Sauropsids and its Importance for Reconstructing Inertial Properties of Extinct
916 Archosaurs. *The Anatomical Record* 292:1442-1461.
- 917 Allmendinger RW, Cardozo NC, and Fisher D. 2013. *Structural Geology Algorithms: Vectors*
918 *and Tensors*. Cambridge: Cambridge University Press.
- 919 Attene M, and Falcidieno B. 2006. ReMESH: An Interactive Environment to Edit and Repair
920 Triangle Meshes. Proceedings of the Eighth International Conference on Shape Modeling
921 and Applications. Matushima. p 271-276.
- 922 Bakker RT. 1986. *The Dinosaur Heresies*. New York: William Morrow & Company, Inc.
- 923 Bates BT, and Schachner ER. 2012. Disparity and convergence in bipedal archosaur locomotion.
924 *Journal of the Royal Society Interface* 9:1339-1353.
- 925 Bates KT, Benson RBJ, and Falkingham PL. 2012. A computational analysis of locomotor
926 anatomy and body mass evolution in Allosauroida (Dinosauria: Theropoda).
927 *Paleobiology* 38:486-507.
- 928 Bates KT, Falkingham PL, Breithaupt BH, Hodgetts D, Sellers WI, and Manning PL. 2009a.
929 How big was 'Big Al'? Quantifying the effect of soft tissue and osteological unknowns on

- 930 mass predictions for *Allosaurus* (Dinosauria: Theropoda). *Palaeontologia Electronica*
931 12:14A.
- 932 Bates KT, Manning PL, Hodgetts D, and Sellers WI. 2009b. Estimating Mass Properties of
933 Dinosaurs Using Laser Imaging and 3D Computer Modelling. *PLoS ONE* 4:e4532.
- 934 Beer FP, Johnston ER, Jr, DeWolf JT, and Mazurek DF. 2012. *Mechanics of Materials*. New
935 York: McGraw-Hill.
- 936 Benson RBJ, Hunt G, Carrano MT, and Campione NE. in press. Cope's Rule and the adaptive
937 landscape of dinosaur body size evolution. *Palaeontology*.
- 938 Biewener AA. 1989. Scaling Body Support in Mammals: Limb Posture and Muscle Mechanics.
939 *Science* 245:45-48.
- 940 Biewener AA. 1990. Biomechanics of Mammalian Terrestrial Locomotion. *Science* 250:1097-
941 1103.
- 942 Biewener AA. 1992. *In vivo* measurement of bone strain and tendon force. In: Biewener AA, ed.
943 *Biomechanics – Structures and Systems: A Practical Approach*. New York: Oxford
944 University Press.
- 945 Bishop KL. 2008. The evolution of flight in bats: narrowing the field of plausible hypotheses.
946 *Quarterly Review of Biology* 83:153-169.
- 947 Bishop PJ, Clemente CJ, Graham DF, Lamas LP, Hutchinson JR, Rubenson J, Hancock JA,
948 Wilson RS, Hocknull SA, Barrett RS, and Lloyd DG. in review-a. The Influence of
949 Speed and Size on Avian Terrestrial Locomotor Biomechanics: Predicting Locomotion in
950 Extinct Theropod Dinosaurs. *PLoS ONE*.
- 951 Bishop PJ, Clemente CJ, Weems RE, Graham DF, Lamas LP, Hutchinson JR, Rubenson J,
952 Wilson RS, Hocknull SA, Barrett RS, and Lloyd DG. 2017. Using step width to compare
953 locomotor biomechanics between extinct, non-avian theropod dinosaurs and modern
954 obligate bipeds. *Journal of the Royal Society Interface* 14:20170276.
- 955 Bishop PJ, Hocknull SA, Clemente CJ, Hutchinson JR, Barrett RS, and Lloyd DG. in review-b.
956 Cancellous bone architecture and theropod dinosaur locomotion. Part II – A new
957 approach to reconstructing posture and locomotor biomechanics in extinct tetrapod
958 vertebrates. *PeerJ*.
- 959 Bishop PJ, Hocknull SA, Clemente CJ, Hutchinson JR, Farke AA, Beck BR, Barrett RS, and
960 Lloyd DG. in review-c. Cancellous bone architecture and theropod dinosaur locomotion.
961 Part I – An examination of cancellous bone architecture in the hindlimb bones of
962 theropods. *PeerJ*.
- 963 Blob RW. 2001. Evolution of hindlimb posture in nonmammalian therapsids: biomechanical
964 tests of paleontological hypotheses. *Paleobiology* 27:14-38.
- 965 Brochu CA. 2003. Osteology of *Tyrannosaurus rex*: insights from a nearly complete skeleton
966 and high-resolution computed tomographic analysis of the skull. *Society of Vertebrate*
967 *Paleontology Memoir* 7:1-138.
- 968 Brusatte SL, Norell MA, Carr TD, Erickson GM, Hutchinson JR, Balanoff AM, Bever GS,
969 Choiniere JN, Makovicky PJ, and Xu X. 2010. Tyrannosaur Paleobiology: New Research
970 on Ancient Exemplar Organisms. *Science* 329:1481-1485.
- 971 Butcher MT, White BJ, Hudzik NB, Gosnell WC, Parrish JHA, and Blob RW. 2011. *In vivo*
972 strains in the femur of the Virginia opossum (*Didelphis virginiana*) during terrestrial
973 locomotion: testing hypotheses of evolutionary shifts in mammalian bone loading and
974 design. *Journal of Experimental Biology* 214:2631-2640.

- 975 Campione NE, Evans DC, Brown CM, and Carrano MT. 2014. Body mass estimation in non-
976 avian bipeds using a theoretical conversion to quadruped stylopodial proportions.
977 *Methods in Ecology and Evolution* 5:913-923.
- 978 Cardozo NC, and Allmendinger RW. 2013. Spherical projections with OSXStereonet.
979 *Computers & Geosciences* 51:193-205.
- 980 Carrano MT. 1998. Locomotion in non-avian dinosaurs: integrating data from hindlimb
981 kinematics, in vivo strains, and bone morphology. *Paleobiology* 24:450-469.
- 982 Carrano MT. 2000. Homoplasy and the evolution of dinosaur locomotion. *Paleobiology* 26:489-
983 512.
- 984 Carrano MT. 2001. Implications of limb bone scaling, curvature and eccentricity in mammals
985 and non-avian dinosaurs. *Journal of Zoology* 254:41-55.
- 986 Carrano MT, and Hutchinson JR. 2002. Pelvic and hindlimb musculature of *Tyrannosaurus rex*
987 (Dinosauria: Theropoda). *Journal of Morphology* 253:207-228.
- 988 Christiansen P. 1998. Strength indicator values of theropod long bones, with comments on limb
989 proportions and cursorial potential. *Gaia* 15:241-255.
- 990 Christiansen P. 1999. Long bone scaling and limb posture in non-avian theropods: evidence for
991 differential allometry. *Journal of Vertebrate Paleontology* 19:666-680.
- 992 Clack JA. 2012. *Gaining Ground: The Origin and Evolution of Tetrapods*. Bloomington: Indiana
993 University Press.
- 994 Dececchi TA, and Larsson HCE. 2013. Body and limb size dissociation at the origin of birds:
995 uncoupling allometric constraints across a macroevolutionary transition. *Evolution*
996 67:2741-2752.
- 997 Delp SL, Anderson FC, Arnold AS, Loan P, Habib A, John CT, Guendelman E, and Thelen DG.
998 2007. OpenSim: Open-Source Software to Create and Analyze Dynamic Simulations of
999 Movement. *IEEE Transactions of Biomedical Engineering* 54:1940-1950.
- 1000 Farlow JO, Chapman RE, Breithaupt BH, and Matthews N. 2012. The Scientific Study of
1001 Dinosaur Footprints. In: Brett-Surman MK, Holtz TR, Jr, and Farlow JO, eds. *The*
1002 *Complete Dinosaur*. 2 ed. Bloomington: Indiana University Press, 712-759.
- 1003 Farlow JO, Smith MB, and Robinson JM. 1995. Body mass, bone "strength indicator," and
1004 cursorial potential of *Tyrannosaurus rex*. *Journal of Vertebrate Paleontology* 15:713-
1005 725.
- 1006 Fujiwara S, and Hutchinson JR. 2012. Elbow joint adductor moment arm as an indicator of
1007 forelimb posture in extinct quadrupedal tetrapods. *Proceedings of the Royal Society of*
1008 *London, Series B* 279:2561-2570.
- 1009 Gao C, Morschhauser EM, Varricchio DJ, Liu J, and Zhao B. 2012. A Second Soundly Sleeping
1010 Dragon: New Anatomical Details of the Chinese Troodontid *Mei long* with Implications
1011 for Phylogeny and Taphonomy. *PLoS ONE* 7:e45203.
- 1012 Gatesy SM. 1990. Caudofemoral musculature and the evolution of theropod locomotion.
1013 *Paleobiology* 16:170-186.
- 1014 Gatesy SM. 1991. Hind Limb Scaling in Birds and Other Theropods: Implications for Terrestrial
1015 Locomotion. *Journal of Morphology* 209:83-96.
- 1016 Gatesy SM. 1994. Neuromuscular Diversity in Archosaur Deep Dorsal Thigh Muscles. *Brain,*
1017 *Behavior and Evolution* 43:1-14.
- 1018 Gatesy SM. 1995. Functional evolution of the hindlimb and tail from basal theropods to birds. In:
1019 Thomason JJ, ed. *Functional Morphology in Vertebrate Paleontology*. New York:
1020 Cambridge University Press, 219-234.

- 1021 Gatesy SM. 1997. An Electromyographic Analysis of Hindlimb Function in *Alligator* During
1022 Terrestrial Locomotion. *Journal of Morphology* 234:197-212.
- 1023 Gatesy SM. 1999a. Guineafowl Hindlimb Function I: Cineradiographic Analysis and Speed
1024 Effects. *Journal of Morphology* 240:115–125.
- 1025 Gatesy SM. 1999b. Guineafowl Hindlimb Function II: Electromyographic Analysis and Motor
1026 Pattern Evolution. *Journal of Morphology* 240:127–142.
- 1027 Gatesy SM. 2002. Locomotor Evolution on the Line to Modern Birds. In: Chiappe LM, and
1028 Witmer LM, eds. *Mesozoic Birds: Above the Heads of the Dinosaurs*. Berkeley:
1029 University of California Press, 432–447.
- 1030 Gatesy SM, Bäker M, and Hutchinson JR. 2009. Constraint-based exclusion of limb poses for
1031 reconstructing theropod dinosaur locomotion. *Journal of Vertebrate Paleontology*
1032 29:535-544.
- 1033 Gatesy SM, and Biewener AA. 1991. Bipedal locomotion: effects of speed, size and limb posture
1034 in birds and humans. *Journal of Zoology* 224:127-147.
- 1035 Gatesy SM, and Middleton KM. 1997. Bipedalism, flight, and the evolution of theropod
1036 locomotor diversity. *Journal of Vertebrate Paleontology* 17:308-329.
- 1037 Gatesy SM, Middleton KM, Jenkins FA, Jr, and Shubin NH. 1999. Three-dimensional
1038 preservation of foot movements in Triassic theropod dinosaurs. *Nature* 399:141-144.
- 1039 Gilmore CW. 1920. Osteology of the carnivorous Dinosauria in the United States National
1040 Museum, with special reference to the genera *Antrodemus* (*Allosaurus*) and
1041 *Ceratosaurus*. *Bulletin of the United States National Museum* 110:1-159.
- 1042 Heers AM, and Dial KP. 2012. From extant to extinct: locomotor ontogeny and the evolution of
1043 avian flight. *Trends in Ecology and Evolution* 27:296-305.
- 1044 Henderson DM. 1999. Estimating the masses and centers of mass of extinct animals by 3-D
1045 mathematical slicing. *Paleobiology* 25:88-106.
- 1046 Henderson DM, and Snively E. 2003. *Tyrannosaurus* en pointe: allometry minimized rotational
1047 inertia of large carnivorous dinosaurs. *Biology Letters* 271:S57-S60.
- 1048 Horner JR, and Lessem D. 1993. *The Complete T. rex*. New York: Simon and Schuster, Inc.
- 1049 Hotton NH, III. 1980. An Alternative to Dinosaur Endothermy: The Happy Wanderers. In:
1050 Thomas RDK, and Olson EC, eds. *A Cold Look at the Warm-Blooded Dinosaurs*.
1051 Boulder: Westview Press, Inc., 311-350.
- 1052 Hutchinson JR. 2001a. The evolution of femoral osteology and soft tissues on the line to extant
1053 birds (Neornithes). *Zoological Journal of the Linnean Society* 131:169-197.
- 1054 Hutchinson JR. 2001b. The evolution of pelvic osteology and soft tissues on the line to extant
1055 birds (Neornithes). *Zoological Journal of the Linnean Society* 131:123-168.
- 1056 Hutchinson JR. 2002. The evolution of hindlimb tendons and muscles on the line to crown-group
1057 birds. *Comparative Biochemistry and Physiology, Part A* 133:1051-1086.
- 1058 Hutchinson JR. 2004. Biomechanical Modeling and Sensitivity Analysis of Bipedal Running
1059 Ability. II. Extinct Taxa. *Journal of Morphology* 262:441-461.
- 1060 Hutchinson JR. 2006. The evolution of locomotion in archosaurs. *Comptes Rendus Palevol*
1061 5:519-530.
- 1062 Hutchinson JR, and Allen V. 2009. The evolutionary continuum of limb function from early
1063 theropods to birds. *Naturwissenschaften* 96:423-448.
- 1064 Hutchinson JR, Anderson FC, Blemker SS, and Delp SL. 2005. Analysis of hindlimb muscle
1065 moment arms in *Tyrannosaurus rex* using a three-dimensional musculoskeletal computer
1066 model: implications for stance, gait, and speed. *Paleobiology* 31:676-701.

- 1067 Hutchinson JR, Bates KT, Molnar J, Allen V, and Makovicky PJ. 2011. A Computational
1068 Analysis of Limb and Body Dimensions in *Tyrannosaurus rex* with Implications for
1069 Locomotion, Ontogeny and Growth. *PLoS ONE* 6:e26037.
- 1070 Hutchinson JR, and Garcia M. 2002. *Tyrannosaurus* was not a fast runner. *Nature* 415:1018-
1071 1021.
- 1072 Hutchinson JR, and Gatesy SM. 2000. Adductors, abductors, and the evolution of archosaur
1073 locomotion. *Paleobiology* 26:734-751.
- 1074 Hutchinson JR, and Gatesy SM. 2006. Dinosaur locomotion: Beyond the bones. *Nature* 440:292-
1075 294.
- 1076 Hutchinson JR, Miller CE, Fritsch G, and Hildebrandt T. 2008. The Anatomical Foundation for
1077 Multidisciplinary Studies of Animal Limb Function: Examples from Dinosaur and
1078 Elephant Limb Imaging Studies. In: Endo H, and Frey R, eds. *Anatomical Imaging:
1079 Towards a New Morphology*. Tokyo: Springer, 23-38.
- 1080 Hutchinson JR, Ng-Thow-Hing V, and Anderson FC. 2007. A 3D interactive method for
1081 estimating body segmental parameters in animals: Application to the turning and running
1082 performance of *Tyrannosaurus rex*. *Journal of Theoretical Biology* 246:660-6800.
- 1083 Jacobson RD, and Hollyday M. 1982. A Behavioural and Electromyographic Study of Walking
1084 in the Chick. *Journal of Neurophysiology* 48:238-256.
- 1085 Johnson RE, and Ostrom JH. 1995. The forelimb of *Torosaurus* and an analysis of the posture
1086 and gait of ceratopsian dinosaurs. In: Thomason JJ, ed. *Functional Morphology in
1087 Vertebrate Paleontology*. Cambridge: Cambridge University Press, 205-218.
- 1088 Kambic RE, Roberts TJ, and Gatesy SM. 2014. Long-axis rotation: a missing degree of freedom
1089 in avian bipedal locomotion. *Journal of Experimental Biology* 217:2770-2782.
- 1090 Kambic RE, Roberts TJ, and Gatesy SM. 2015. Guineafowl with a twist: asymmetric limb
1091 control in steady bipedal locomotion. *Journal of Experimental Biology* 218:3836-3844.
- 1092 Keller TS, and Spengler DM. 1989. Regulation of bone stress and strain in the immature and
1093 mature rat femur. *Journal of Biomechanics* 22:1115-1127.
- 1094 Kemp TS. 1982. *Mammal-like Reptiles and the Origin of Mammals*. London: Academic Press.
- 1095 Lambe LM. 1917. The Cretaceous theropodous dinosaur Gorgosaurus. *Memoirs of the
1096 Geological Survey of Canada* 100:1-84.
- 1097 Lautenschlager S. 2016. Reconstructing the past: methods and techniques for the digital
1098 restoration of fossils. *Royal Society Open Science* 3:160342.
- 1099 Lee MSY, Cau A, Naish D, and Dyke GJ. 2014. Sustained miniaturization and anatomical
1100 innovation in the dinosaurian ancestors of birds. *Science* 345:562-566.
- 1101 Marsh RL, Ellerby DJ, Carr JA, Henry HT, and Buchanan CI. 2004. Partitioning the Energetics
1102 of Walking and Running: Swinging the Limbs is Expensive. *Science* 303:80-83.
- 1103 Martelli S, Taddei F, Testi D, Delp SL, and Viceconti M. 2011. NMSBuilder: an application to
1104 personalize NMS models. Proceedings of the 23rd Congress of the International Society
1105 of Biomechanics. Brussels.
- 1106 McCrea RT, Buckley LG, Farlow JO, Lockley MG, Currie PJ, Matthews NA, and Pemberton
1107 SG. 2014. A 'Terror of Tyrannosaurs': The First Trackways of Tyrannosaurids and
1108 Evidence of Gregariousness and Pathology in Tyrannosauridae. *PLoS ONE* 9:e103613.
- 1109 Molnar RE, and Farlow JO. 1990. Carnosaur Paleobiology. In: Weishampel DB, Dodson P, and
1110 Osmólska H, eds. *The Dinosauria*. 1 ed. Berkeley: University of California Press, 210-
1111 224.

- 1112 Norell MA, and Makovicky PJ. 1997. Important Features of the Dromaeosaur Skeleton:
1113 Information from a New Specimen. *American Museum Novitates* 3215:1-28.
- 1114 Norell MA, and Makovicky PJ. 1999. Important Features of the Dromaeosaurid Skeleton II:
1115 Information from Newly Collected Specimens of *Velociraptor mongoliensis*. *American*
1116 *Museum Novitates* 3282:1-45.
- 1117 Osborn HF. 1917. Skeletal adaptations of *Ornitholestes*, *Struthiomimus*, *Tyrannosaurus*. *Bulletin*
1118 *of the American Museum of Natural History* 35:733-771.
- 1119 Ostrom JH. 1969. Osteology of *Deinonychus antirrhopus*, and unusual theropod from the Lower
1120 Cretaceous of Montana. *Bulletin of the Peabody Museum of Natural History* 30:1-165.
- 1121 Paul GS. 1998. Limb design, function and running performance in ostrich-mimics and
1122 tyrannosaurs. *Gaia* 15:257-270.
- 1123 Pauwels F. 1980. *Biomechanics of the Locomotor Apparatus*. Berlin: Springer-Verlag.
- 1124 Pierce SE, Hutchinson JR, and Clack JA. 2013. Historical Perspectives on the Evolution of
1125 Tetrapodomorph Movement. *Integrative and Comparative Biology* 53:209-223.
- 1126 Pittman M, Gatesy SM, Upchurch P, Goswami A, and Hutchinson JR. 2013. Shake a Tail
1127 Feather: The Evolution of the Theropod Tail into a Stiff Aerodynamic Surface. *PLoS*
1128 *ONE* 8:e63115.
- 1129 Rauhut OWM, and Carrano MT. 2016. The theropod dinosaur *Elaphrosaurus bambergi*
1130 Janensch, 1920, from the Late Jurassic of Tendaguru, Tanzania. *Zoological Journal of the*
1131 *Linnean Society* 178:546-610.
- 1132 Reilly SM, and Blob RW. 2003. Motor control of locomotor hindlimb posture in the American
1133 alligator (*Alligator mississippiensis*). *Journal of Experimental Biology* 206:4327-4340.
- 1134 Roberts TJ, Chen MS, and Taylor CR. 1998. Energetics of bipedal running. II. Limb design and
1135 running mechanics. *Journal of Experimental Biology* 205:2753-2762.
- 1136 Rubenson J, Lloyd DG, Besier TF, Heliams DB, and Fournier PA. 2007. Running in ostriches
1137 (*Struthio camelus*): three-dimensional joint axes alignment and joint kinematics. *Journal*
1138 *of Experimental Biology* 210:2548-2562.
- 1139 Sellers WI, and Manning PL. 2007. Estimating dinosaur maximum running speeds using
1140 evolutionary robotics. *Proceedings of the Royal Society of London, Series B* 274:2711-
1141 2716.
- 1142 Sellers WI, Pond SB, Brassey CA, Manning PL, and Bates KT. 2017. Investigating the running
1143 abilities of *Tyrannosaurus rex* using stress-constrained multibody dynamic analysis.
1144 *PeerJ* 5:e3420.
- 1145 Stevens KA, and Parrish JM. 2005. Digital Reconstructions of Sauropod Dinosaurs and
1146 Implications for Feeding. In: Curry Rogers KA, and Wilson JA, eds. *The Sauropods:*
1147 *Evolution and Paleobiology*. Berkeley: University of California Press, 178-200.
- 1148 Taylor MP, Wedel MJ, and Naish D. 2009. Head and neck posture in sauropod dinosaurs
1149 inferred from extant animals. *Acta Palaeontologica Polonica* 54:213-220.
- 1150 Thewissen JGM, and Babcock SK. 1992. The Origin of Flight in Bats. *BioScience* 42:340-345.
- 1151 Thulborn T. 1990. *Dinosaur Tracks*. London: Chapman and Hall.
- 1152 Tsai HP, and Holliday CM. 2015. Articular Soft Tissue Anatomy of the Archosaur Hip Joint:
1153 Structural Homology and Functional Implications. *Journal of Morphology* 276:601-630.
- 1154 Tsuihiji T, Barsbold R, Watabe M, Tsogtbaatar K, Chinzorig T, Fujiyama Y, and Suzuki S.
1155 2014. An exquisitely preserved troodontid theropod with new information on the palatal
1156 structure from the Upper Cretaceous of Mongolia. *Naturwissenschaften* 101:131-142.
- 1157 Unwin DM. 2005. *The Pterosaurs: From Deep Time*. New York: Pi Press.

- 1158 Valente G, Pitto L, Testi D, Seth A, Delp SL, Stagni R, Viceconti M, and Taddei F. 2014. Are
1159 Subject-Specific Musculoskeletal Models Robust to the Uncertainties in Parameter
1160 Identification? *PLoS ONE* 9:e112625.
- 1161 van der Reest AJ, and Currie PJ. 2017. Troodontids (Theropoda) from the Dinosaur Park
1162 Formation, Alberta, with a description of a unique new taxon: implications for
1163 deinonychosaur diversity in North America. *Canadian Journal of Earth Sciences* 54:919-
1164 935.
- 1165 Villette CC. 2016. Structural Meso and Microscale Finite Element Based Approaches for the
1166 prediction of Bone Architecture and Fracture PhD. Imperial College London.
- 1167 Wall-Scheffler CM, Chumanov E, Steudel-Numbers K, and Heiderscheid B. 2010.
1168 Electromyography Activity Across Gait and Incline: The Impact of Muscular Activity on
1169 Human Morphology. *American Journal of Physical Anthropology* 143:601-611.
- 1170 Xu X, Norell MA, Wang X, Makovicky PJ, and Wu X. 2002. A basal troodontid from the Early
1171 Cretaceous of China. *Nature* 415:780-784.
- 1172 Xu X, Zhou Z, Dudley R, Mackem S, Chuong C-M, Erickson GM, and Varricchio DJ. 2014. An
1173 integrative approach to understanding bird origins. *Science* 346:1253293.
- 1174 Zelenitsky DK, Therrien F, Erickson GM, DeBuhr CL, Kobayashi Y, Eberth DA, and Hadfield
1175 F. 2012. Feathered Non-Avian Dinosaurs from North America Provide Insight into Wing
1176 Origins. *Science* 338:510-514.

1177

1178

1179 **III.9 Figure captions**

1180

1181

1182 **Figure 1.** The musculoskeletal model of the *Daspletosaurus* hindlimb developed in this study.
1183 This is shown in the ‘neutral posture’ for all joints, that is, when all joint angles are zero. (A–C)
1184 Geometries of the musculotendon actuators in relation to the bones, in lateral (A), anterior (B)
1185 and oblique anterolateral (C) views. (D–F) Location and orientation of joint coordinate systems
1186 (red, green and blue axes), the centres of mass for each segment (grey and white balls) and the
1187 soft tissue volumes used to calculate mass properties; these are shown in the same views as A–C.
1188 Also reported in D are the masses for each segment. In D–F, the flexion-extension axis of each
1189 joint is the blue axis. For scale, the length of each arrow in the triad of the global coordinate
1190 system is 500 mm.

1191

1192

1193 **Figure 2.** The musculoskeletal model of the ‘*Troodon*’ hindlimb developed in this study. This is
1194 shown in the neutral posture for all joints. (A–C) Geometries of the musculotendon actuators in

1195 relation to the bones, in lateral (A), anterior (B) and oblique anterolateral (C) views. (D–F)
1196 Location and orientation of joint coordinate systems (red, green and blue axes), the centres of
1197 mass for each segment (grey and white balls) and the soft tissue volumes used to calculate mass
1198 properties; these are shown in the same views as A–C. Also reported in D are the masses for each
1199 segment. In D–F, the flexion-extension axis of each joint is the blue axis. For scale, the length of
1200 each arrow in the triad of the global coordinate system is 200 mm.

1201

1202

1203 **Figure 3.** Varying the articulation of the hip joint in the *Daspletosaurus* model. (A, B) The
1204 original ‘solution posture’ identified for the *Daspletosaurus* model. (C, D) The first variation in
1205 hip articulation, where the femur (and limb distal to it) is moved medially by 50 mm. (E, F) The
1206 second variation in hip articulation, where the femur (and limb distal to it) is moved medially by
1207 50 mm, also with a sizeable amount of hip abduction and external long-axis rotation. A, C and E
1208 are in oblique anterolateral view; B, D and F are in anterior view. Intervening soft tissues used in
1209 the finite element simulations are shown in turquoise; for clarity, the ilium and pubis are shown
1210 translucent in B, D and F. Also illustrated in B are the relative diameters of the femoral head
1211 (solid lines) and the acetabulum (dashed lines).

1212

1213

1214 **Figure 4.** The identified solution postures for *Daspletosaurus* and ‘*Troodon*’. (A, B) Calculated
1215 angular deviation between the minimum principal stress (σ_3) and the mean direction of the
1216 primary fabric orientation (\mathbf{u}_1) in the femoral head (grey bars) and medial femoral condyle (white
1217 bars) for each posture tested, for *Daspletosaurus* (A) and ‘*Troodon*’ (B). This shows the
1218 progressive improvement in alignment between stresses and cancellous bone architecture across
1219 the postures tested. (C–E) The solution posture for *Daspletosaurus* in lateral (C), dorsal (D) and
1220 anterior (E) views. (F–H) The solution posture for ‘*Troodon*’ in lateral (F), dorsal (G) and
1221 anterior (H) views. Also illustrated in C and F are stick figure representations of the other
1222 postures tested, and the whole-body COM of the solution posture. The solution postures resulted
1223 in the greatest degree of overall correspondence between principal stress trajectories and
1224 observed cancellous bone architectural patterns, as assessed by qualitative comparisons across the

1225 femur, tibiotarsus and fibula, as well as quantitative results for the femoral head and medial
1226 femoral condyle.

1227

1228

1229 **Figure 5.** Principal stress trajectories for the proximal femur in the solution posture of
1230 *Daspletosaurus*, compared with observed cancellous bone fabric. For easier visual comparison,
1231 these stress trajectories were ‘downsampled’ in a custom MATLAB script, by interpolating the
1232 raw stress results at each finite element node to a regular grid. (A) Vector field of σ_1 (red) and σ_3
1233 (blue) in a 3-D slice through the proximal femur, parallel to the coronal plane and through the
1234 middle of the femoral head, in anterior view. Note how the trajectory of σ_3 projects towards the
1235 apex of the femoral head (green braces). (B) Geometric representation of cancellous bone
1236 architecture in the proximal femur of *Allosaurus* and tyrannosaurids (cf. Part I), in the same view
1237 as A. (C) Vector field of σ_1 and σ_3 in a 3-D slice through the lesser trochanter, parallel to the
1238 plane of the trochanter, in anterolateral view. (D) Geometric representation of cancellous bone
1239 architecture in the lesser trochanter of *Allosaurus* and tyrannosaurids (cf. Part I), in the same view
1240 as C. (E) Vector field of σ_3 in the femoral head, shown as a 3-D slice parallel to the sagittal plane
1241 and through the apex of the head, in medial view. (F) Geometric representation of cancellous
1242 bone architecture in the femoral head of *Allosaurus* and tyrannosaurids (cf. Part I), in the same
1243 view as E. (G) Comparison of the mean direction of σ_3 in the femoral head (blue) and the
1244 estimated mean direction of \mathbf{u}_1 for *Allosaurus* and tyrannosaurids (red), plotted on an equal-angle
1245 stereoplot with northern hemisphere projection (using StereoNet 9.5; Allmendinger et al. 2013;
1246 Cardozo & Allmendinger 2013). Inset shows location of region for which the mean direction of
1247 σ_3 was calculated.

1248

1249

1250 **Figure 6.** Principal stress trajectories for the distal femur and fourth trochanter in the solution
1251 posture of *Daspletosaurus*, compared with observed cancellous bone fabric. (A) Vector field of
1252 σ_1 (red) and σ_3 (blue) in a 3-D slice, parallel to the coronal plane and through the anterior aspect
1253 of the distal metaphysis, in anterior view. (B) Geometric representation of cancellous bone
1254 architecture in the distal metaphysis of *Allosaurus* and tyrannosaurids (cf. Part I), in the same
1255 view as A. (C) Vector field of σ_1 in the fourth trochanter, in medial view. (D) Geometric

1256 representation of cancellous bone architecture in the fourth trochanter of *Allosaurus* and
1257 tyrannosaurids (cf. Part I), in the same view as C. (E) Vector field of σ_3 in the lateral condyle,
1258 shown as a 3-D slice parallel to the sagittal plane and through the middle of the condyle. (F)
1259 Geometric representation of cancellous bone architecture in the lateral condyle of *Allosaurus* and
1260 tyrannosaurids (cf. Part I), in the same view as E. (G) Vector field of σ_3 in the medial condyle,
1261 shown as a 3-D slice parallel to the sagittal plane and through the middle of the condyle. (H)
1262 Geometric representation of cancellous bone architecture in the medial condyle of *Allosaurus* and
1263 tyrannosaurids (cf. Part I), in the same view as G. (I) Comparison of the mean direction of σ_3 in
1264 the medial condyle (blue) and the estimated mean direction of u_1 for *Allosaurus* and
1265 tyrannosaurids (red), plotted on an equal-angle stereoplot with southern hemisphere projection.
1266 Inset shows location of region for which the mean direction of σ_3 was calculated.

1267

1268

1269 **Figure 7.** Principal stress trajectories for the tibia and fibula in the solution posture for
1270 *Daspletosaurus*, compared with observed cancellous bone fabric. (A) Vector field of σ_3 in the
1271 medial tibial condyle, shown as a 3-D slice through the middle of the condyle and parallel to the
1272 sagittal plane, in medial view. (B) Geometric representation of cancellous bone architecture in the
1273 medial tibial condyle of *Allosaurus* and tyrannosaurids (cf. Part I), in the same view as A. (C)
1274 Vector field of σ_3 in the medial and lateral tibial condyles, shown as 3-D slices through the
1275 middle of the condyles and parallel to the coronal plane, in posterior view. (D) Geometric
1276 representation of cancellous bone architecture in the medial and lateral tibial condyles of
1277 *Allosaurus* and tyrannosaurids (cf. Part I), in the same view as C. (E) Vector field of σ_3 in the
1278 lateral tibial condyle, shown as a 3-D slice through the middle of the condyle and parallel to the
1279 sagittal plane, in lateral view. (F) Geometric representation of cancellous bone architecture in the
1280 lateral tibial condyle of *Allosaurus* and tyrannosaurids (cf. Part I), in the same view as E. (G)
1281 Vector field of σ_1 in the cnemial crest, shown as a 3-D slice parallel to the coronal plane, in
1282 anterior view. (H) Geometric representation of cancellous bone architecture in cnemial crest of
1283 *Allosaurus* and tyrannosaurids (cf. Part I), sectioned in the plane of the crest, shown in the same
1284 view as G; blue section lines illustrate primary architectural direction. (I) Vector field of σ_1 in the
1285 cnemial crest, shown as a 3-D slice parallel to the sagittal plane, in medial view. (J) Geometric
1286 representation of cancellous bone architecture in cnemial crest of *Allosaurus* and tyrannosaurids

1287 (cf. Part I), sectioned in the plane of the crest, shown in the same view as I. (K) Vector field of σ_3
1288 in the medial aspect of the fibular head, in medial view. (L) Geometric representation of
1289 cancellous bone architecture in the fibular head of *Allosaurus* and tyrannosaurids (cf. Part I), in
1290 the same view as K.

1291

1292

1293 **Figure 8.** Principal stress trajectories for the proximal femur in the solution posture of ‘*Troodon*’,
1294 compared with observed cancellous bone fabric. (A, B) Vector field of σ_3 in the femoral head,
1295 shown as 3-D slices parallel to the coronal plane (A, in anterior view) and sagittal plane (B, in
1296 medial view). (C, D) Vector field of u_1 in the femoral head, in the same views as A and B,
1297 respectively (cf. Part I). (E) Comparison of the mean direction of σ_3 in the femoral head (blue)
1298 and the mean direction of u_1 (red), plotted on an equal-angle stereoplot with northern hemisphere
1299 projection. Inset shows location of region for which the mean direction of σ_3 was calculated. (F,
1300 G) Vector field of σ_3 under the greater trochanter, shown as 3-D slices parallel to the coronal
1301 plane (F, in posterior view) and sagittal plane (G, in lateral view). (H, I) Vector field of u_1 under
1302 the greater trochanter, shown in the same views as F and G, respectively (cf. Part I). (J) Vector
1303 field of σ_1 in the lesser trochanter, shown in oblique anterolateral view. (K) Vector field of u_1 in
1304 the lesser trochanter, shown in the same view as J for both specimens studied (cf. Part I).

1305

1306

1307 **Figure 9.** Principal stress trajectories for the distal femoral condyles in the solution posture of
1308 ‘*Troodon*’, compared with observed cancellous bone fabric. (A) Vector field of σ_3 in the lateral
1309 condyle, shown as a 3-D slice parallel to the sagittal plane. (B) Vector field of u_1 in the lateral
1310 condyle, shown in the same view as A (cf. Part I). (C) Vector field of σ_3 in the medial condyle,
1311 shown as a 3-D slice parallel to the sagittal plane. (D) Vector field of u_1 in the medial condyle,
1312 shown in the same view as C (cf. Part I). (E) Comparison of the mean direction of σ_3 in the
1313 medial condyle (blue) and the mean direction of u_1 (red), plotted on an equal-angle stereoplot
1314 with southern hemisphere projection. This shows that in the solution posture the mean direction
1315 of σ_3 was of the same general azimuth as the mean direction of u_1 , but was markedly more
1316 posteriorly inclined. Inset shows location of region for which the mean direction of σ_3 was
1317 calculated.

1318

1319

1320 **Figure 10.** Principal stress trajectories for the tibia and fibula in the solution posture for
1321 ‘*Troodon*’, compared with observed cancellous bone fabric. (A) Vector field of σ_3 in the medial
1322 tibial condyle, shown as a 3-D slice through the middle of the condyle and parallel to the sagittal
1323 plane, in medial view. (B) Vector field of u_1 in the medial tibial condyle, in the same view as A
1324 (cf. Part I). (C) Vector field of σ_3 in the medial and lateral tibial condyles, shown as 3-D slices
1325 through the middle of the condyles and parallel to the coronal plane, in posterior view. (D)
1326 Vector field of u_1 in the medial and lateral tibial condyles, in the same view as C (cf. Part I). (E)
1327 Vector field of σ_3 in the lateral tibial condyle, shown as a 3-D slice through the middle of the
1328 condyle and parallel to the sagittal plane, in lateral view. (F) Vector field of u_1 in the lateral tibial
1329 condyle, in the same view as E (cf. Part I). (G) Vector field of σ_1 in the cnemial crest, shown as a
1330 3-D slice parallel to the coronal plane, in anterior view. (H) Vector field of u_1 in the cnemial
1331 crest, in the same view as G (cf. Part I). (I) Vector field of σ_1 in the cnemial crest, shown as a 3-D
1332 slice parallel to the sagittal plane, in medial view. (J) Vector field of u_1 in the cnemial crest, in
1333 the same view as I (cf. Part I). (K) Vector field of σ_1 in the lateral fibular head, in lateral view.
1334 (L) Vector field of σ_3 in the medial fibular head, in medial view (reversed). (M) Vector field of u_1
1335 in the fibular head, in the same view as K (cf. Part I).

1336

1337

1338 **Figure 11.** Principal stress trajectories for the proximal femur of *Daspletosaurus* in the two
1339 variations in hip articulation tested. (A) Vector field of σ_3 in the first variation tested, shown as a
1340 3-D slice parallel to the coronal plane and through the middle of the femoral head. (B) Vector
1341 field of σ_3 in the first variation tested, shown as a 3-D slice parallel to the sagittal plane and
1342 through the apex of the femoral head. (C) Vector field of σ_3 in the second variation tested, shown
1343 as a 3-D slice parallel to the coronal plane and through the middle of the femoral head. (D)
1344 Vector field of σ_3 in the second variation tested, shown as a 3-D slice parallel to the sagittal plane
1345 and through the apex of the femoral head. A and C are in anterior view, B and D are in medial
1346 view. Note in particular how the trajectory of σ_3 projects towards the more cylindrical part of the
1347 femoral head, lateral to the apex (green braces); compare to [Fig. 5A,B,E,F](#). Also note in C how σ_3
1348 has a strong medial component near the apex of the head.

1349

1350

1351 **Figure 12.** Comparison of parameters related to posture, extracted from the solution postures of
1352 the three species modelled: *Daspletosaurus* ('D'), 'Troodon' ('T') and the chicken ('C'). (A)
1353 Schematic illustration of the solution postures retrieved for the three species, along with the
1354 location of the whole-body centre of mass (black and white disc). (B) Whole-body centre of mass
1355 location anterior to the hips, normalized to total leg length. (C) Degree of crouch for each species,
1356 both as measured from the solution posture, as well as empirically predicted from the data
1357 reported by Bishop et al. (in review-a). (D) Angles of the hip and knee joints. The hip extension
1358 angle is expressed relative to the horizontal, whereas the knee flexion angle is expressed relative
1359 to the femur. (E) Long-axis rotation and adduction-abduction of the hip joint. Positive values
1360 indicate external rotation and abduction (respectively), whereas negative values indicate internal
1361 rotation and adduction (respectively).

1362

1363

1364 **Figure 13.** Comparison of parameters related to bone loading mechanics and muscular support,
1365 extracted from the solution postures of the three species modelled: *Daspletosaurus* ('D'),
1366 'Troodon' ('T') and the chicken ('C'). (A) Orientation of the neutral axis of bending and the
1367 orientation of principal stresses (σ_1 and σ_3) relative to the femur long-axis, both measured at mid-
1368 shaft. Insets show the neutral axis with respect to the mid-shaft cross-section, as well as
1369 anatomical directions (A, anterior; P, posterior; M, medial; L, lateral). (B) Ratio of maximum
1370 shear to bending stress in the femoral mid-shaft. (C) Normalized moments of hip abductor and
1371 medial rotator muscles. The hip abductor for all species is the iliofemoralis externus (activation
1372 set to zero in the chicken; see Part II). In *Daspletosaurus* and 'Troodon', the medial rotators are
1373 the iliotrochantericus caudalis and puboischiofemorales internus 1 et 2; in the chicken, they are
1374 the iliotrochanterici caudalis et medius. (D) Oblique anterolateral view of the hip of
1375 *Daspletosaurus*, showing the abductor and medial rotator muscles (colour codes as in C).

1376

Table 1 (on next page)

The specimens utilized in building the models of *Daspletosaurus torosus* and ' *Troodon* ', as well as the settings used to acquire CT scans.

The geometry of specimens that were not CT scanned was captured via digital photogrammetry.

Table 1. The specimens utilized in building the models of *Daspletosaurus torosus* and ‘*Troodon*’. Also listed are the settings used in acquiring CT scans; the geometry of specimens that were not CT scanned was captured via digital photogrammetry.

Higher-order taxonomy	Species	Specimen number*	Element	CT scan settings					
				Machine	Peak tube voltage (kV)	Tube current (mA)	Exposure time (ms)	In-plane pixel resolution (mm)	Slice thickness (mm)
Coelurosauria, Tyrannosauridae	<i>Albertosaurus sarcophagus</i>	TMP 81.010.0001	Pubis						
Coelurosauria, Tyrannosauridae	<i>Albertosaurus sarcophagus</i>	TMP 81.010.0001	Ischium						
Coelurosauria, Tyrannosauridae	<i>Gorgosaurus libratus</i>	TMP 1994.012.0603	Metatarsals II–IV + distal tarsals	GE Lightspeed Ultra	140	150	1195	0.703	1.25
Coelurosauria, Tyrannosauridae	<i>Daspletosaurus torosus</i>	TMP 2001.036.0001	Femur	GE Lightspeed Ultra	140	150	1195	0.838	1.25
Coelurosauria, Tyrannosauridae	<i>Daspletosaurus torosus</i>	TMP 2001.036.0001	Tibia	GE Lightspeed Ultra	120	245	1195	0.832	1.25
Coelurosauria, Tyrannosauridae	<i>Daspletosaurus torosus</i>	TMP 2001.036.0001	Fibula	GE Lightspeed Ultra	120	245	1195	0.832	1.25
Coelurosauria, Tyrannosauridae	<i>Daspletosaurus torosus</i>	TMP 2001.036.0001	Astragalus	GE Lightspeed Ultra	140	155	1195	0.879	1.25
Coelurosauria, Tyrannosauridae	<i>Daspletosaurus torosus</i>	TMP 2001.036.0001	Metatarsal IV + lateral distal tarsal	GE Lightspeed Ultra	120	185	1195	0.738	1.25
Coelurosauria, Tyrannosauridae	<i>Daspletosaurus torosus</i>	TMP 2001.036.0001	Ilium						
Coelurosauria, Tyrannosauridae	<i>Daspletosaurus torosus</i>	TMP 2001.036.0001	Pubis						
Coelurosauria, Tyrannosauridae	<i>Daspletosaurus torosus</i>	TMP 2001.036.0001	Ischium						
Coelurosauria, Tyrannosauridae	<i>Tyrannosaurus rex</i>	MOR 009	Metatarsal V	Toshiba Aquilion 64	135	250	750	0.625	0.5
Coelurosauria, Tyrannosauridae	<i>Daspletosaurus horneri</i>	MOR 590	Metatarsals II–IV + phalanges						
Coelurosauria, Tyrannosauridae	<i>Tyrannosaurus rex</i>	MOR 980	Pubis						

Table 1 (continued).

Higher-order taxonomy	Species	Specimen number*	Element	CT scan settings					
				Machine	Peak tube voltage (kV)	Tube current (mA)	Exposure time (ms)	In-plane pixel resolution (mm)	Slice thickness (mm)
Coelurosauria, Tyrannosauridae	<i>Tyrannosaurus rex</i>	MOR 980	Ischium						
Coelurosauria, Tyrannosauridae	<i>Daspletosaurus horneri</i>	MOR 1130	Calcaneum	Toshiba Aquilion 64	135	150	1000	0.526	0.5
Coelurosauria, Tyrannosauridae	<i>Daspletosaurus horneri</i>	MOR 1130	Metatarsal I	Toshiba Aquilion 64	135	150	1000	0.526	0.5
Coelurosauria, Tyrannosauridae	<i>Teratophoneus curriei</i>	UMNH VP 16690	Pubis						
Coelurosauria, Tyrannosauridae	<i>Teratophoneus curriei</i>	UMNH VP 16690	Ischium						
Paraves, Troodontidae	<i>Latenivenatrix mcmastrae</i>	TMP 1992.036.0575	Metatarsals II–V	Siemens Inveon	80	250	1700	0.05	0.05
Paraves, Troodontidae	sp.	MOR 553I-7.27.8.67	Ischium						
Paraves, Troodontidae	sp.	MOR 553s-7.11.91.41	Tibia	Siemens Inveon	80	200	1900	0.04	0.04
Paraves, Troodontidae	sp.	MOR 553s-7.28.91.239	Femur	Siemens Inveon	80	200	1800	0.04	0.04
Paraves, Troodontidae	sp.	MOR 553s-8.3.9.387	Pubis						
Paraves, Troodontidae	sp.	MOR 553s-8.6.92.168	Metatarsal I						
Paraves, Troodontidae	sp.	MOR 553s-8.17.92.265	Fibula	Siemens Inveon	80	250	1600	0.04	0.04
Paraves, Troodontidae	sp.	MOR 748	Femur	Siemens Inveon	80	200	1900	0.04	0.04
Paraves, Troodontidae	sp.	MOR 748	Tibia + astragalus + calcaneum	Siemens Inveon	80	200	1900	0.04	0.04
Paraves, Troodontidae	sp.	MOR 748	Metatarsals II–IV	Siemens Inveon	80	200	1900	0.04	0.04
Paraves, Troodontidae	sp.	MOR 748	Ilium						
Paraves, Troodontidae	sp.	MOR uncatalogued	Ilium						

*Collection number abbreviations: MOR, Museum of the Rockies; TMP, Royal Tyrrell Museum of Palaeontology; UMNH VP; Natural History Museum of Utah.

Table 2 (on next page)

The origins and insertions of each of the muscles and ligaments represented in the *Daspletosaurus* and '*Troodon*' musculoskeletal models.

Specific differences between the two theropods are noted where appropriate.

Table 2. The origins and insertions of each of the muscles and ligaments represented in the *Daspletosaurus* and ‘*Troodon*’ musculoskeletal models. Specific differences between the two theropods are noted where appropriate.

Muscle or ligament	Abbreviation	Origin	Insertion
Iliotibialis 1	IT1	Anterior rim of lateral ilium	Cnemial crest
Iliotibialis 2	IT2	Dorsal rim of ilium, lateral surface	Cnemial crest
Iliotibialis 3	IT3	Dorsal rim of postacetabular ilium	Cnemial crest
Ambiens	AMB	Preacetabular process on proximal pubis	Cnemial crest
Femorotibialis externus	FMTE	Lateral femoral shaft	Cnemial crest
Femorotibialis internus	FMTI	Anteromedial femoral shaft	Cnemial crest
Iliofibularis	ILFB	Lateral postacetabular ilium, between IFE and FTE; posterior to median vertical ridge of the ilium in <i>Daspletosaurus</i>	Fibular tubercle
Iliofemoralis externus	IFE	Lateral ilium, anterodorsal to acetabulum; anterior to median vertical ridge of the ilium in <i>Daspletosaurus</i>	Trochanteric shelf of femur
Iliotrochantericus caudalis	ITC	Lateral preacetabular ilium	Lesser trochanter
Puboischiofemoralis internus 1	PIF1	Iliac preacetabular fossa; also descending onto lateral surface of pubic peduncle in <i>Daspletosaurus</i>	Anteromedial aspect of proximal femur
Puboischiofemoralis internus 2	PIF2	Near PIF1 origin, probably anterior to it (iliac preacetabular fossa)	Distal to lesser trochanter; on accessory trochanter in <i>Daspletosaurus</i>
Flexor tibialis internus 1	FTI1	Low tubercle on posterolateral ischial shaft in <i>Daspletosaurus</i> ; distal end of ischium in ‘ <i>Troodon</i> ’	Medial proximal tibia
Flexor tibialis internus 3	FTI3	Ischial tuberosity on posterolateral proximal ischium in <i>Daspletosaurus</i> ; proximal ischial shaft in ‘ <i>Troodon</i> ’	Medial proximal tibia
Flexor tibialis externus	FTE	Lateral postacetabular ilium	Medial proximal tibia
Adductor femoris 1	ADD1	Lateral surface of obturator process	Medial posterodistal surface of femoral shaft; large scarred region in <i>Daspletosaurus</i>
Adductor femoris 2	ADD2	Posterodorsal rim of ischium	Lateral posterodistal surface of femoral shaft; large scarred region in <i>Daspletosaurus</i>
Puboischiofemoralis externus 1	PIFE1	Anterior surface of pubic apron	Greater trochanter
Puboischiofemoralis externus 2	PIFE2	Posterior surface of pubic apron	Greater trochanter
Puboischiofemoralis externus 3	PIFE3	Lateral ischium, between ADD1 and ADD2	Greater trochanter
Ischiotrochantericus	ISTR	Medial surface of ischium	Lateral proximal femur

Table 2 (continued).

Muscle or ligament	Abbreviation	Origin	Insertion
Caudofemoralis longus	CFL	Caudal vertebral centra, probably from caudal vertebrae 1–15 in <i>Daspletosaurus</i> and caudal vertebrae 1–10 in <i>Troodon</i>	Medial surface of fourth trochanter in <i>Daspletosaurus</i> , posteromedial surface of proximal femur in <i>Troodon</i>
Caudofemoralis brevis	CFB	Brevis fossa of ilium	Lateral surface of fourth trochanter in <i>Daspletosaurus</i> , posterolateral surface of proximal femur in <i>Troodon</i>
Gastrocnemius lateralis	GL	Posterolateral surface of distal femur	Posterior surface of metatarsals II-IV
Gastrocnemius medialis	GM	Medial proximal tibia	Posterior surface of metatarsals II-IV
Flexor digitorum longus	FDL	Posterior surface of distal femur	Ventral aspect of digit II-IV phalanges
Flexor digitorum brevis	FDB	Posterior surface of metatarsals II-IV	Ventral aspect of digit II-IV phalanges
Flexor hallucis longus	FHL	Posterior surface of femur	Ventral aspect of digit I phalanges
Extensor digitorum longus	EDL	Distal anterolateral femur; possibly also proximal anterior tibia in <i>Daspletosaurus</i> , and possibly also distal anterolateral femur in <i>Troodon</i>	Dorsal aspect of digit II-IV phalanges
Extensor digitorum brevis	EDB	Anterior surface of metatarsals	Dorsal aspect of digit II-IV phalanges
Extensor hallucis longus	EHL	Distal fibula	Dorsal aspect of digit I ungual
Tibialis anterior	TA	Anterior surface of proximal tibia	Anteroproximal metatarsals II-IV
Fibularis longus	FL	Anterolateral surface of tibia and/or fibula	Posterolateral ankle region (e.g., metatarsal V)
Fibularis brevis	FB	Distal to FL on fibula	Anterolateral ankle region (e.g., metatarsal IV)
Knee medial collateral ligament	KMCL	Depression on medial surface of medial femoral condyle	Medial proximal tibiotarsus, proximal to FCLP and FCM insertions
Knee lateral collateral ligament	KLCL	Lateral surface of lateral femoral condyle	Lateral fibular head
Ankle medial collateral ligament	AMCL	Depression on medial surface of astragalus	Medial proximal tarsometatarsus
Ankle lateral collateral ligament	ALCL	Depression on lateral surface of calcaneum	Lateral proximal tarsometatarsus

Table 3(on next page)

Hypothetical activities of the muscle actuators used in the *Daspletosaurus* and '*Troodon*' simulations.

X = active (capable of exerting up to two body weights of force), O = inactive (exerts zero force).

Table 3. Hypothetical activities of the muscle actuators used in the *Daspletosaurus* and ‘*Troodon*’ simulations. X = active (capable of exerting up to two body weights of force), O = inactive (exerts zero force).

Muscle	Activity
IT1	X
IT2	X
IT3	X
AMB	X
FMTE	X
FMTI	X
ILFB	X
IFE	X
ITC	X
PIFI1	X
PIFI2	X
FTI1	X
FTI3	X
FTE	X
ADD1	X
ADD2	X
PIFE1	O
PIFE2	O
PIFE3	O
ISTR	X
CFL	X
CFB	X
GL	X
GM	X
FDL	X
FDB	X
FHL	X
EDL	O
EDB	O
EHL	O
TA	O
FL	O
FB	O

Figure 1(on next page)

The musculoskeletal model of the Daspletosaurus hindlimb developed in this study.

This is shown in the 'neutral posture' for all joints, that is, when all joint angles are zero.

(A-C) Geometries of the musculotendon actuators in relation to the bones, in lateral (A), anterior (B) and oblique anterolateral (C) views. (D-F) Location and orientation of joint coordinate systems (red, green and blue axes), the centres of mass for each segment (grey and white balls) and the soft tissue volumes used to calculate mass properties; these are shown in the same views as A-C. Also reported in D are the masses for each segment. In D-F, the flexion-extension axis of each joint is the blue axis. For scale, the length of each arrow in the triad of the global coordinate system is 500 mm.

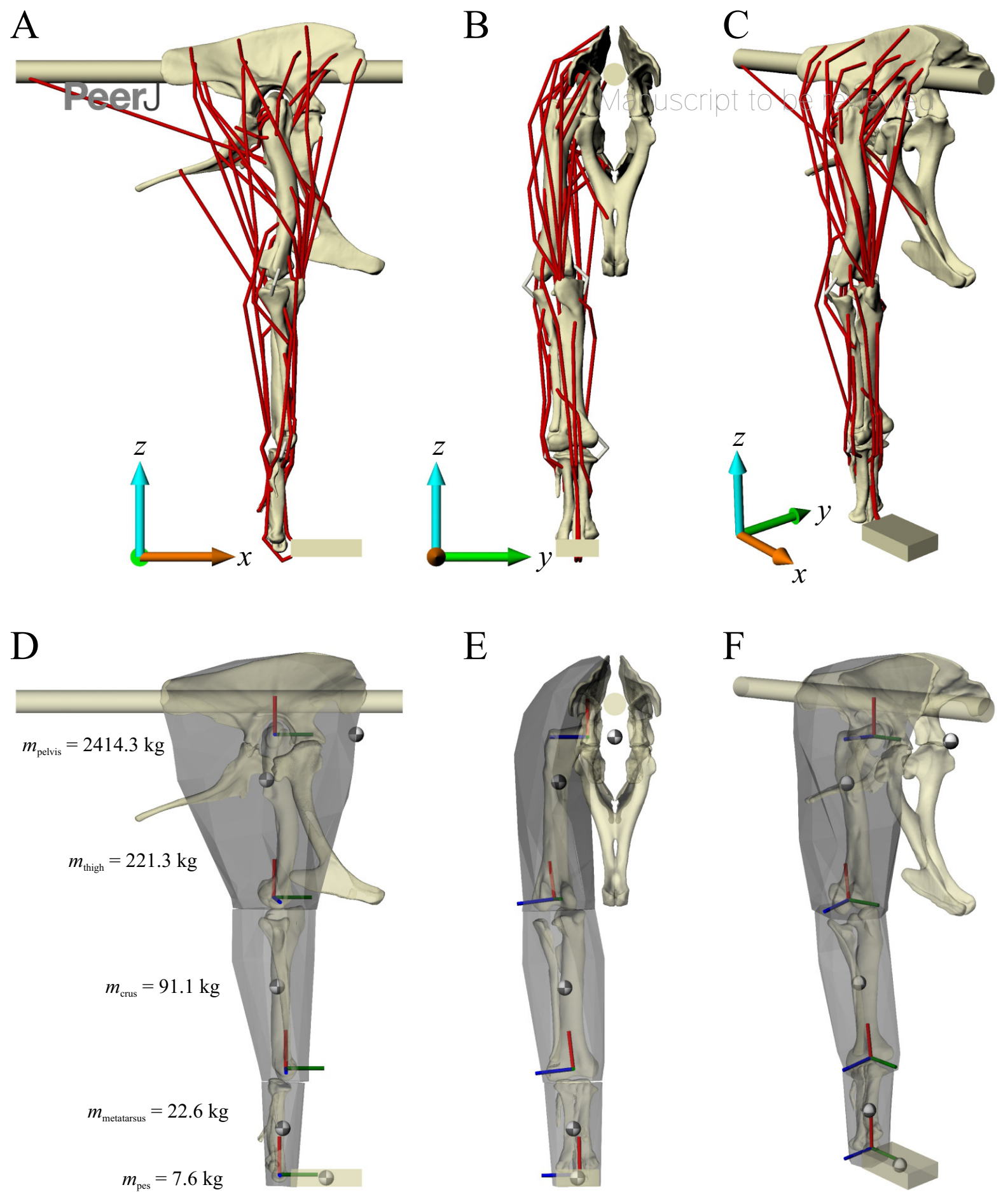


Figure 2(on next page)

The musculoskeletal model of the 'Troodon' hindlimb developed in this study.

This is shown in the neutral posture for all joints. (A-C) Geometries of the musculotendon actuators in relation to the bones, in lateral (A), anterior (B) and oblique anterolateral (C) views. (D-F) Location and orientation of joint coordinate systems (red, green and blue axes), the centres of mass for each segment (grey and white balls) and the soft tissue volumes used to calculate mass properties; these are shown in the same views as A-C. Also reported in D are the masses for each segment. In D-F, the flexion-extension axis of each joint is the blue axis. For scale, the length of each arrow in the triad of the global coordinate system is 200 mm.

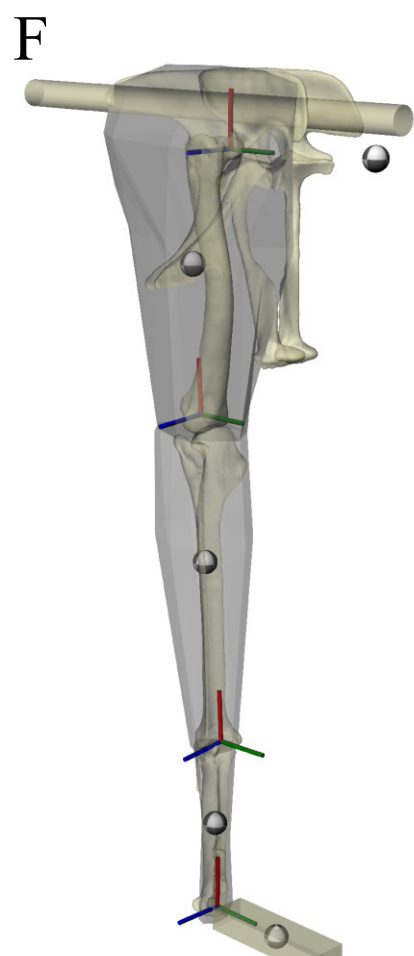
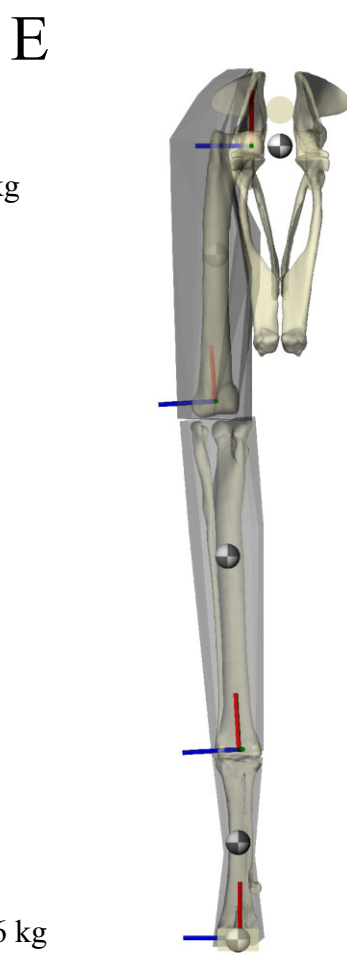
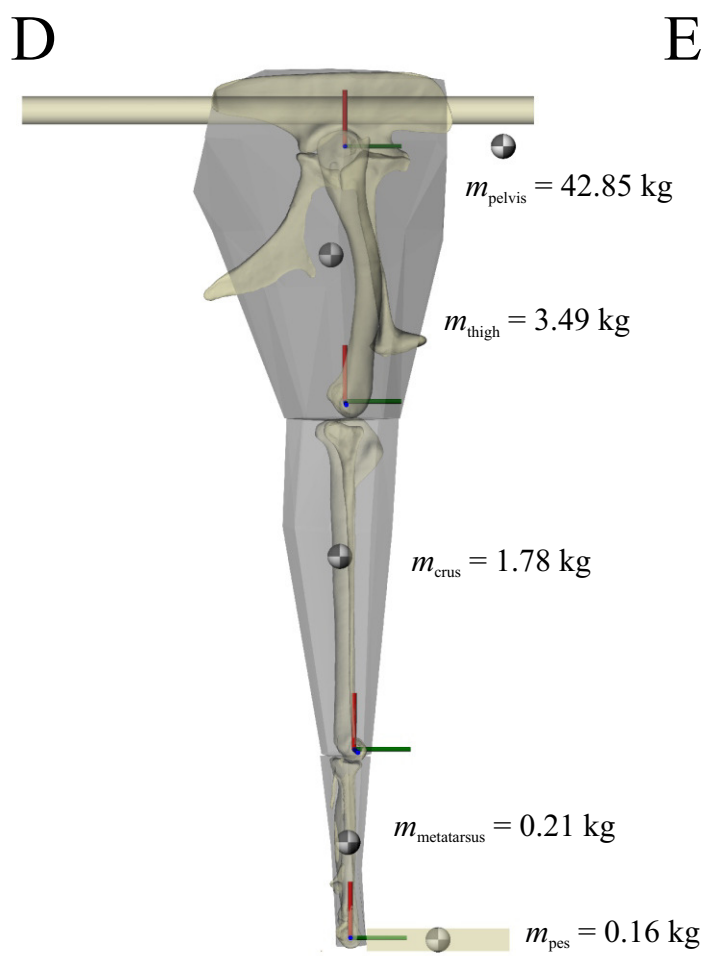
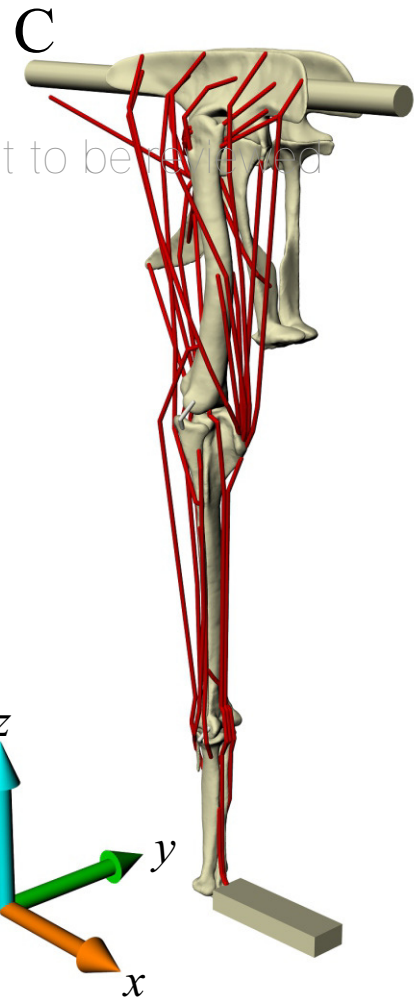
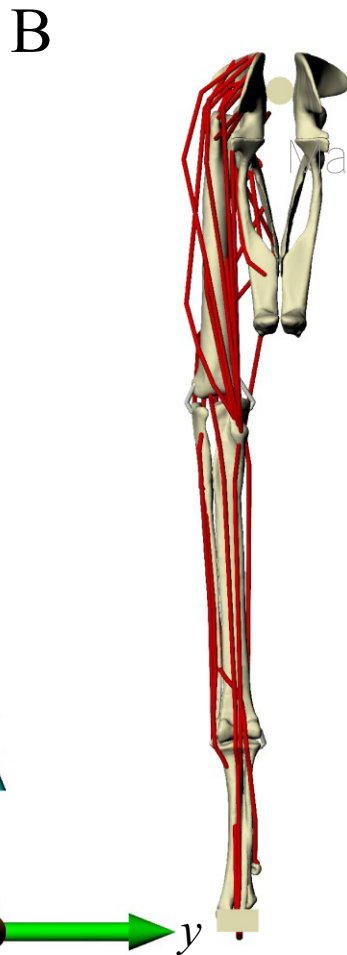
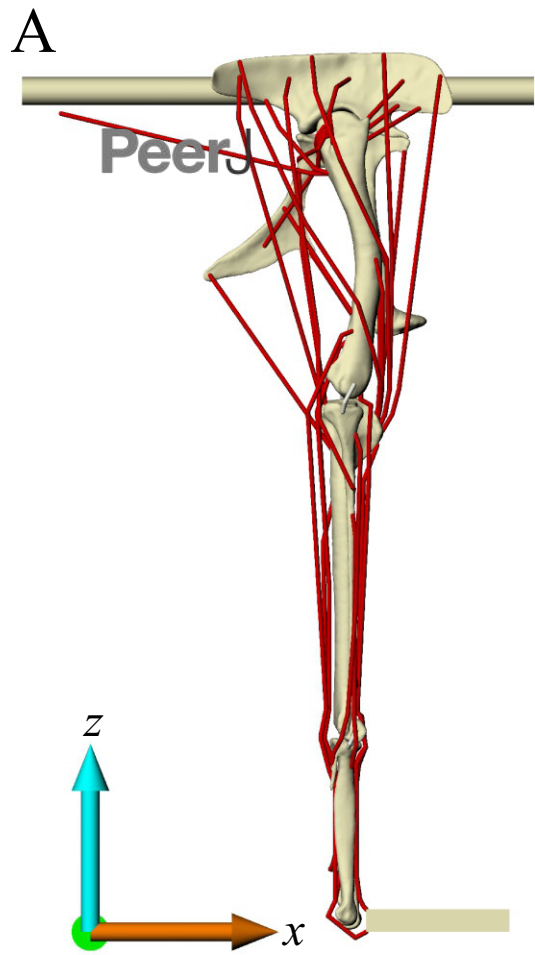
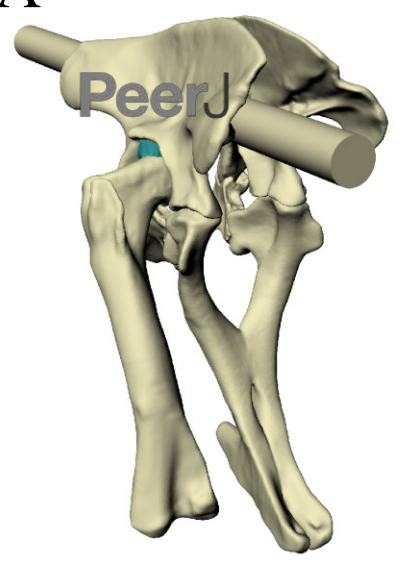


Figure 3(on next page)

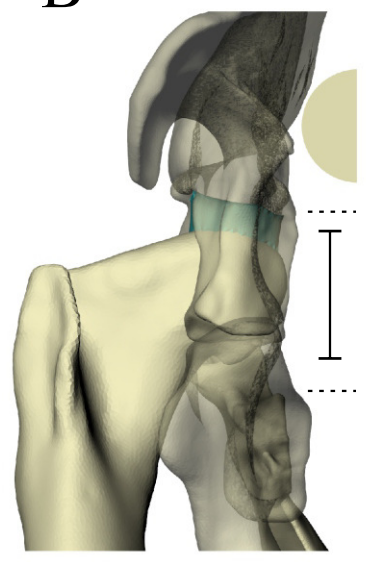
Varying the articulation of the hip joint in the Daspletosaurus model.

(A, B) The original 'solution posture' identified for the Daspletosaurus model. (C, D) The first variation in hip articulation, where the femur (and limb distal to it) is moved medially by 50 mm. (E, F) The second variation in hip articulation, where the femur (and limb distal to it) is moved medially by 50 mm, also with a sizeable amount of hip abduction and external long-axis rotation. A, C and E are in oblique anterolateral view; B, D and F are in anterior view. Intervening soft tissues used in the finite element simulations are shown in turquoise; for clarity, the ilium and pubis are shown translucent in B, D and F. Also illustrated in B are the relative diameters of the femoral head (solid lines) and the acetabulum (dashed lines).

A

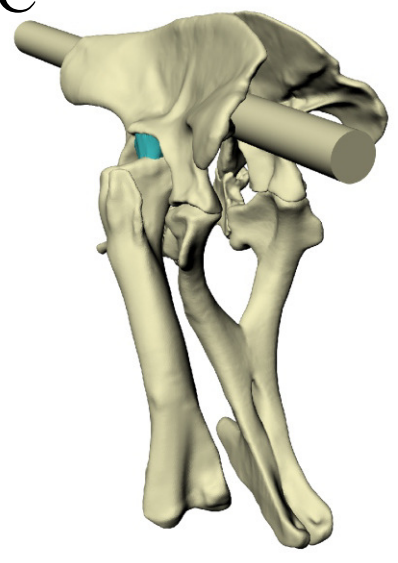


B

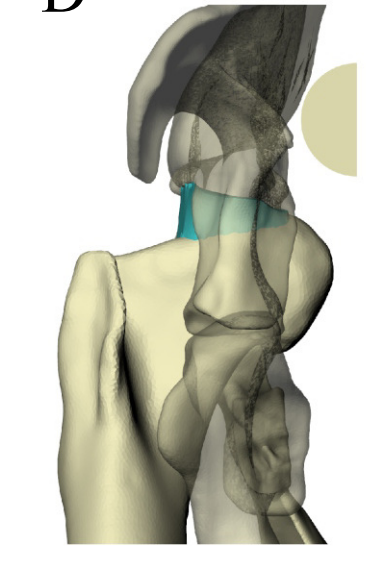


Manuscript to be reviewed

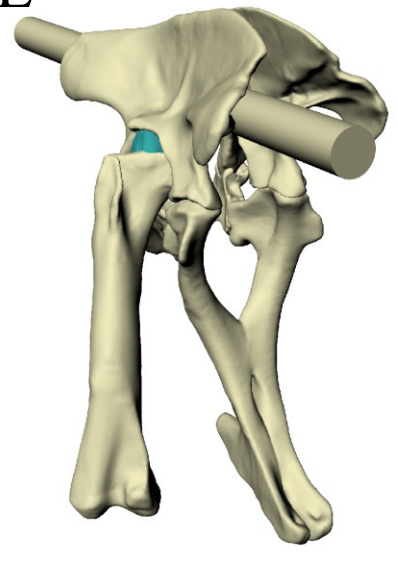
C



D



E



F

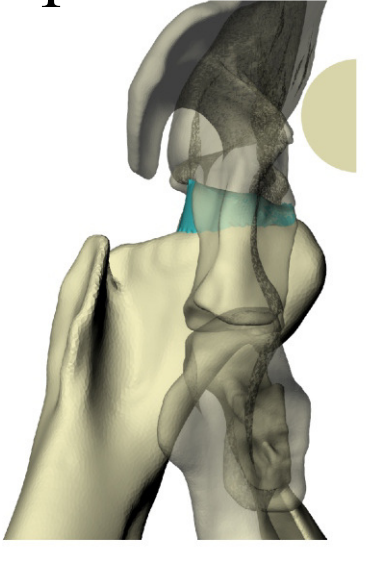


Figure 4(on next page)

The identified solution postures for Daspletosaurus and ' Troodon '.

(A, B) Calculated angular deviation between the minimum principal stress (σ_3) and the mean direction of the primary fabric orientation (u_1) in the femoral head (grey bars) and medial femoral condyle (white bars) for each posture tested, for Daspletosaurus (A) and ' Troodon ' (B). This shows the progressive improvement in alignment between stresses and cancellous bone architecture across the postures tested. (C-E) The solution posture for Daspletosaurus in lateral (C), dorsal (D) and anterior (E) views. (F-H) The solution posture for ' Troodon ' in lateral (F), dorsal (G) and anterior (H) views. Also illustrated in C and F are stick figure representations of the other postures tested, and the whole-body COM of the solution posture. The solution postures resulted in the greatest degree of overall correspondence between principal stress trajectories and observed cancellous bone architectural patterns, as assessed by qualitative comparisons across the femur, tibiotarsus and fibula, as well as quantitative results for the femoral head and medial femoral condyle.

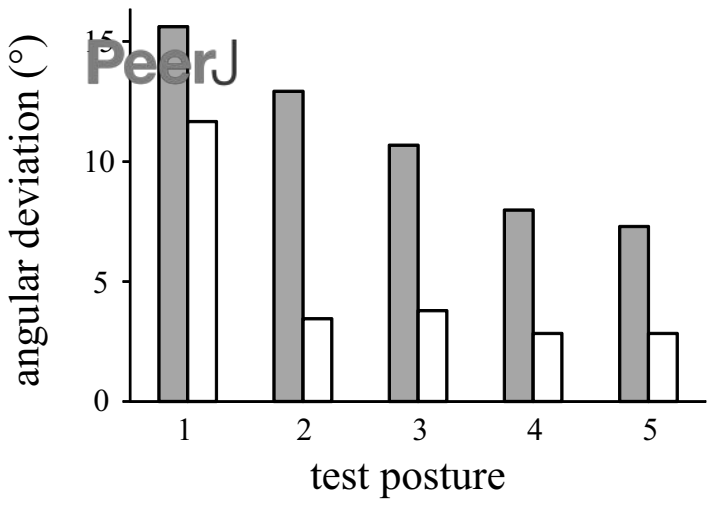
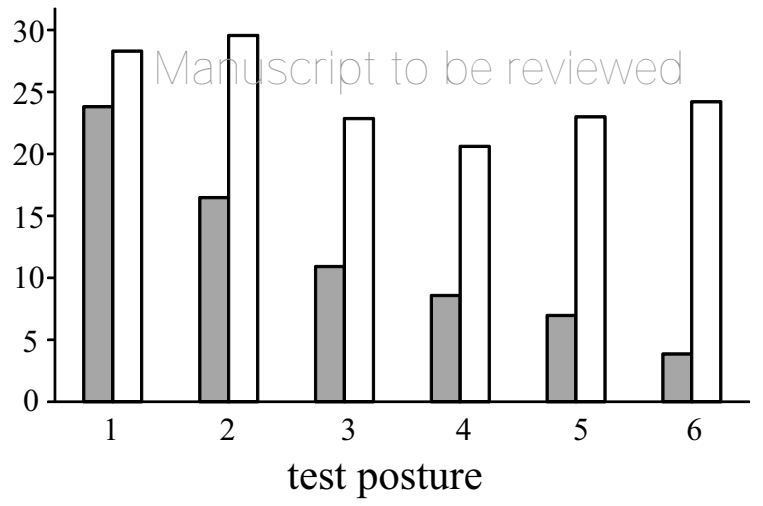
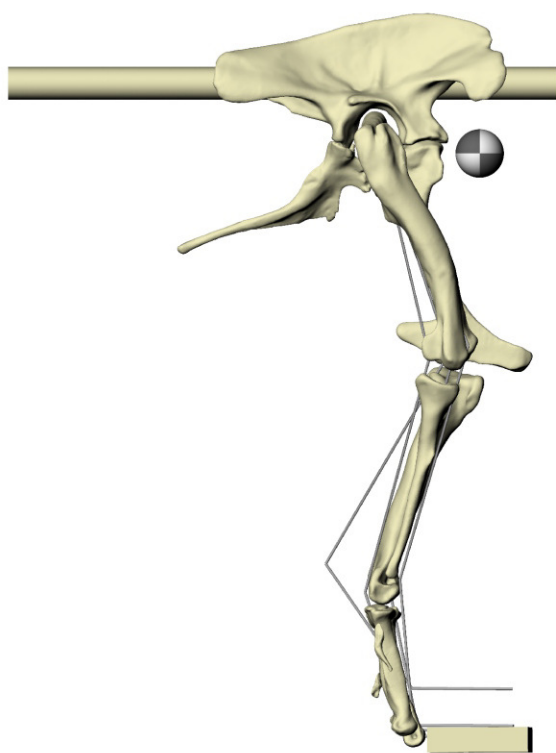
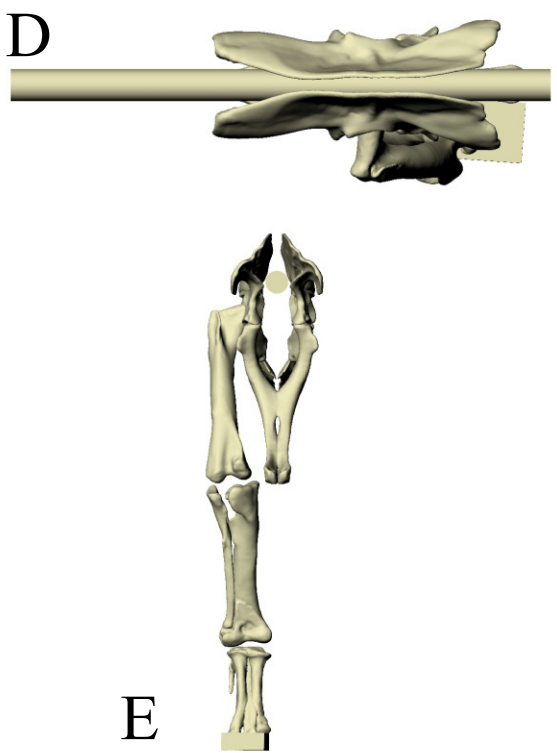
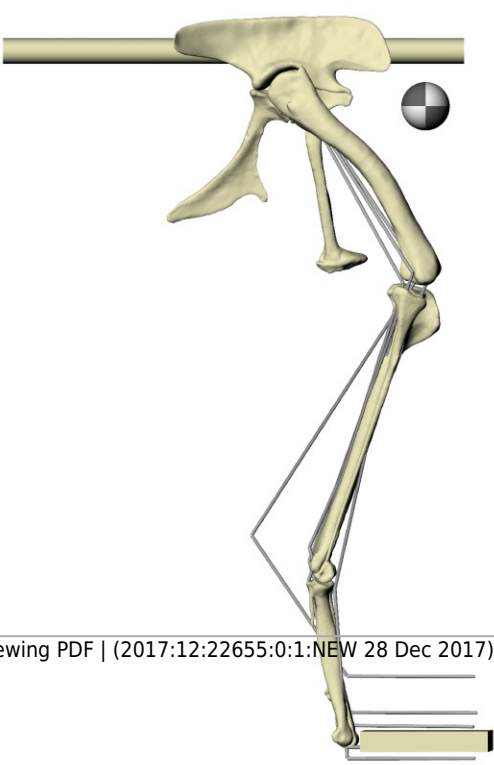
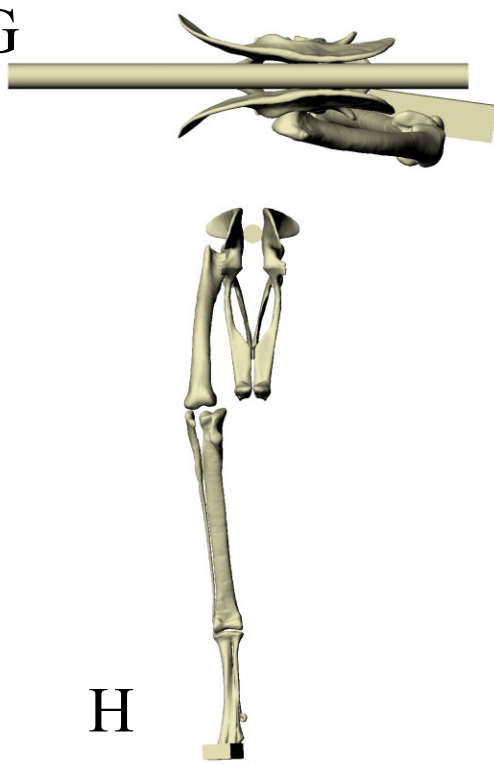
A**B****C****D****F****G****H**

Figure 5(on next page)

Principal stress trajectories for the proximal femur in the solution posture of *Daspletosaurus*, compared with observed cancellous bone fabric.

For easier visual comparison, these stress trajectories were 'downsampled' in a custom MATLAB script, by interpolating the raw stress results at each finite element node to a regular grid. (A) Vector field of σ_1 (red) and σ_3 (blue) in a 3-D slice through the proximal femur, parallel to the coronal plane and through the middle of the femoral head, in anterior view. Note how the trajectory of σ_3 projects towards the apex of the femoral head (green braces). (B) Geometric representation of cancellous bone architecture in the proximal femur of *Allosaurus* and tyrannosaurids (cf. Part I), in the same view as A. (C) Vector field of σ_1 and σ_3 in a 3-D slice through the lesser trochanter, parallel to the plane of the trochanter, in anterolateral view. (D) Geometric representation of cancellous bone architecture in the lesser trochanter of *Allosaurus* and tyrannosaurids (cf. Part I), in the same view as C. (E) Vector field of σ_3 in the femoral head, shown as a 3-D slice parallel to the sagittal plane and through the apex of the head, in medial view. (F) Geometric representation of cancellous bone architecture in the femoral head of *Allosaurus* and tyrannosaurids (cf. Part I), in the same view as E. (G) Comparison of the mean direction of σ_3 in the femoral head (blue) and the estimated mean direction of u_1 for *Allosaurus* and tyrannosaurids (red), plotted on an equal-angle stereoplot with northern hemisphere projection (using StereoNet 9.5; Allmendinger et al. 2013; Cardozo & Allmendinger 2013). Inset shows location of region for which the mean direction of σ_3 was calculated.

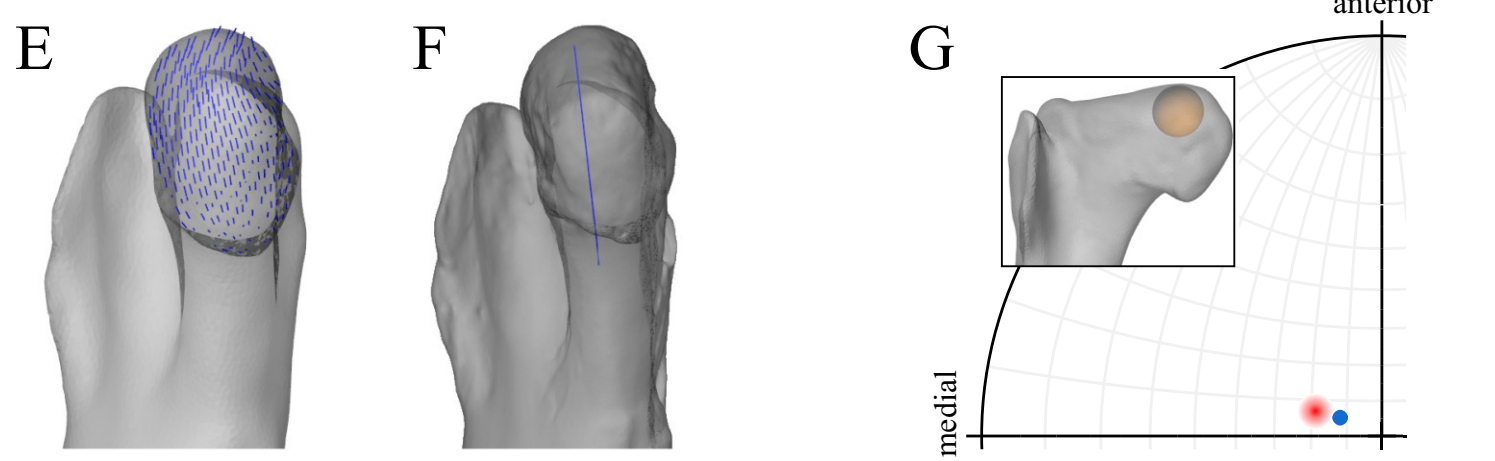
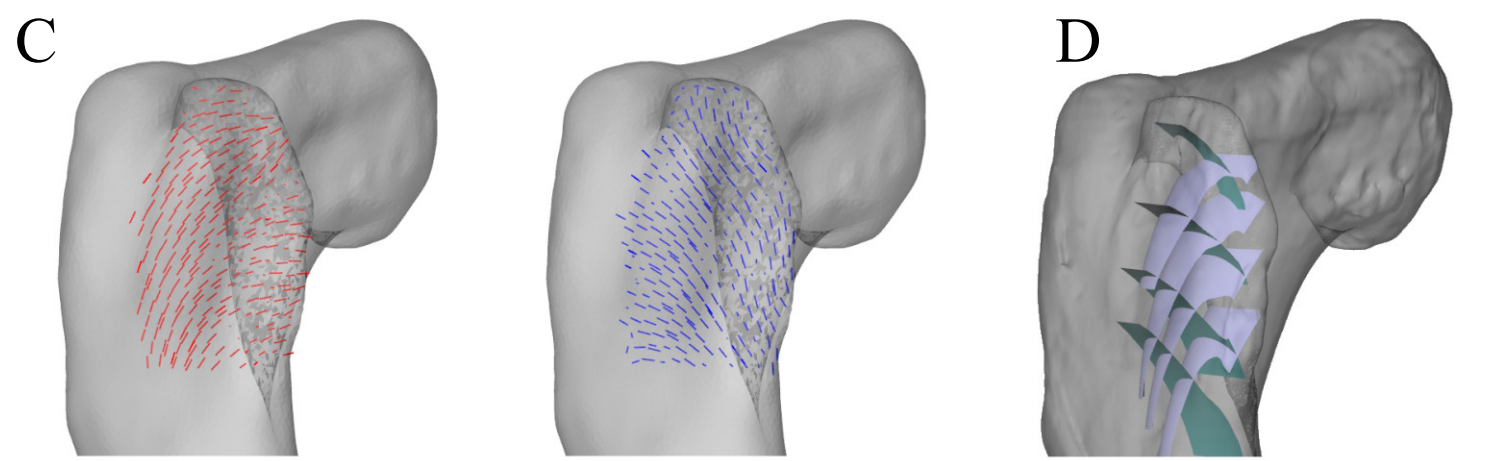
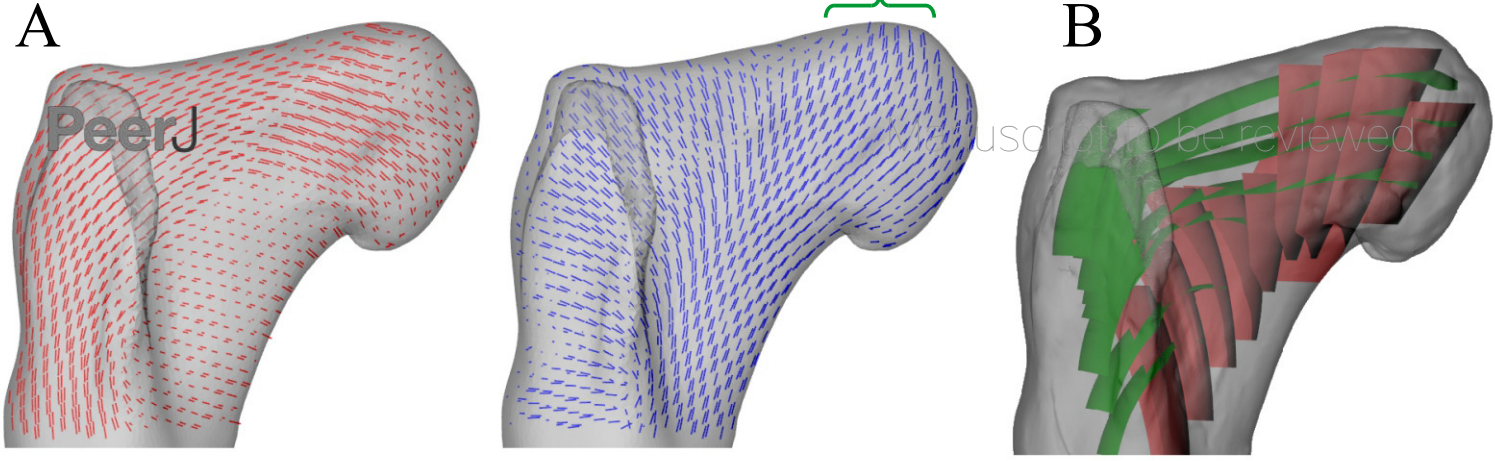


Figure 6(on next page)

Principal stress trajectories for the distal femur and fourth trochanter in the solution posture of *Daspletosaurus*, compared with observed cancellous bone fabric.

(A) Vector field of σ_1 (red) and σ_3 (blue) in a 3-D slice, parallel to the coronal plane and through the anterior aspect of the distal metaphysis, in anterior view. (B) Geometric representation of cancellous bone architecture in the distal metaphysis of *Allosaurus* and tyrannosaurids (cf. Part I), in the same view as A. (C) Vector field of σ_1 in the fourth trochanter, in medial view. (D) Geometric representation of cancellous bone architecture in the fourth trochanter of *Allosaurus* and tyrannosaurids (cf. Part I), in the same view as C. (E) Vector field of σ_3 in the lateral condyle, shown as a 3-D slice parallel to the sagittal plane and through the middle of the condyle. (F) Geometric representation of cancellous bone architecture in the lateral condyle of *Allosaurus* and tyrannosaurids (cf. Part I), in the same view as E. (G) Vector field of σ_3 in the medial condyle, shown as a 3-D slice parallel to the sagittal plane and through the middle of the condyle. (H) Geometric representation of cancellous bone architecture in the medial condyle of *Allosaurus* and tyrannosaurids (cf. Part I), in the same view as G. (I) Comparison of the mean direction of σ_3 in the medial condyle (blue) and the estimated mean direction of u_1 for *Allosaurus* and tyrannosaurids (red), plotted on an equal-angle stereoplot with southern hemisphere projection. Inset shows location of region for which the mean direction of σ_3 was calculated.

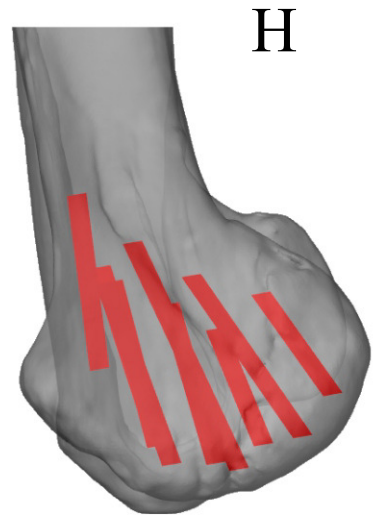
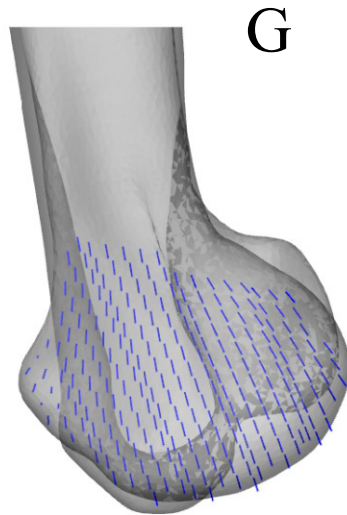
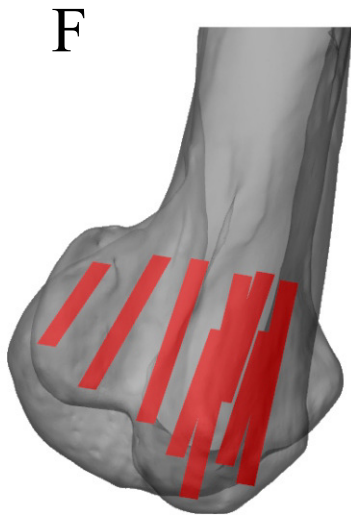
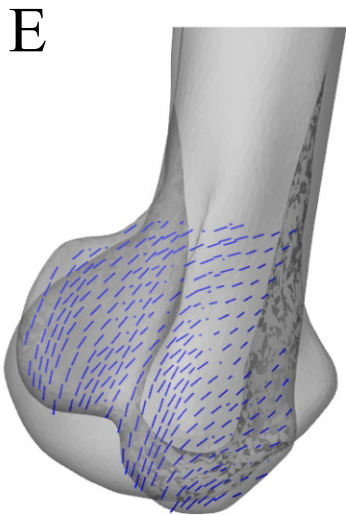
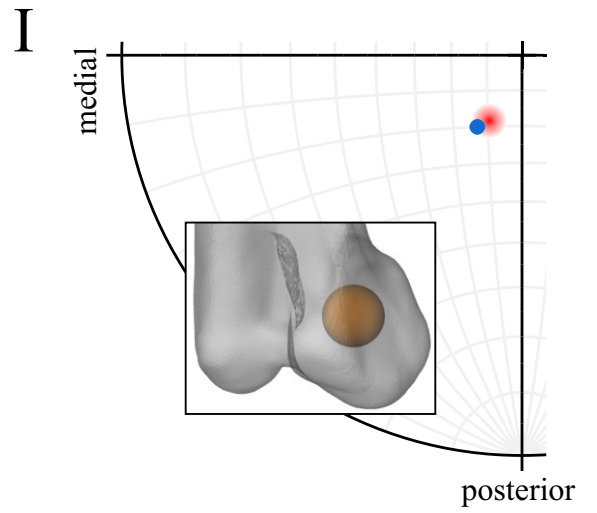
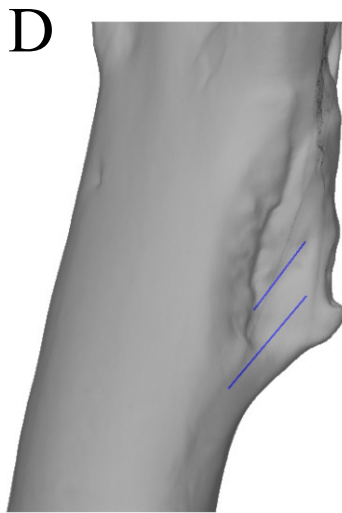
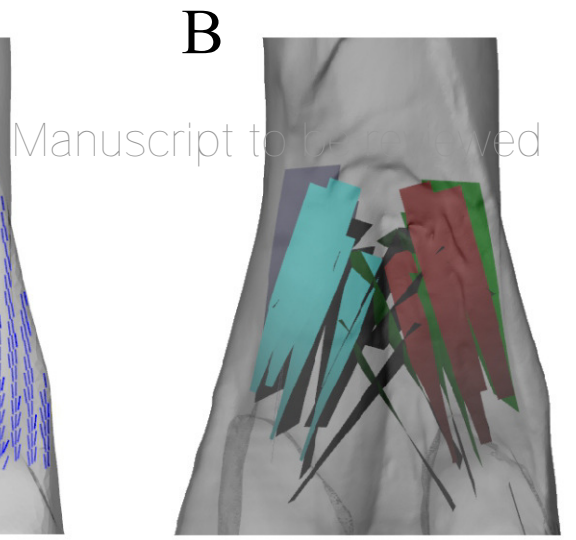
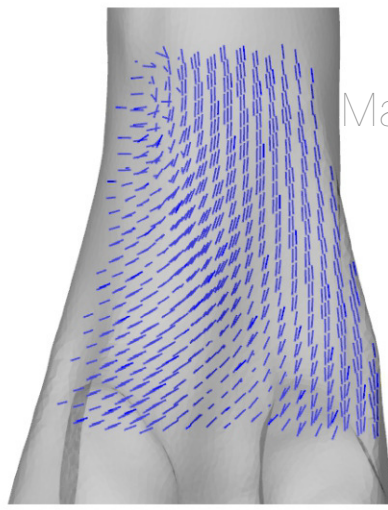
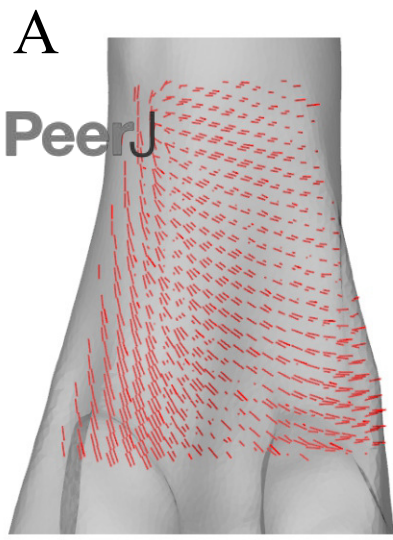


Figure 7 (on next page)

Principal stress trajectories for the tibia and fibula in the solution posture for *Daspletosaurus*, compared with observed cancellous bone fabric.

(A) Vector field of σ_3 in the medial tibial condyle, shown as a 3-D slice through the middle of the condyle and parallel to the sagittal plane, in medial view. (B) Geometric representation of cancellous bone architecture in the medial tibial condyle of *Allosaurus* and tyrannosaurids (cf. Part I), in the same view as A. (C) Vector field of σ_3 in the medial and lateral tibial condyles, shown as 3-D slices through the middle of the condyles and parallel to the coronal plane, in posterior view. (D) Geometric representation of cancellous bone architecture in the medial and lateral tibial condyles of *Allosaurus* and tyrannosaurids (cf. Part I), in the same view as C. (E) Vector field of σ_3 in the lateral tibial condyle, shown as a 3-D slice through the middle of the condyle and parallel to the sagittal plane, in lateral view. (F) Geometric representation of cancellous bone architecture in the lateral tibial condyle of *Allosaurus* and tyrannosaurids (cf. Part I), in the same view as E. (G) Vector field of σ_1 in the cnemial crest, shown as a 3-D slice parallel to the coronal plane, in anterior view. (H) Geometric representation of cancellous bone architecture in cnemial crest of *Allosaurus* and tyrannosaurids (cf. Part I), sectioned in the plane of the crest, shown in the same view as G; blue section lines illustrate primary architectural direction. (I) Vector field of σ_1 in the cnemial crest, shown as a 3-D slice parallel to the sagittal plane, in medial view. (J) Geometric representation of cancellous bone architecture in cnemial crest of *Allosaurus* and tyrannosaurids (cf. Part I), sectioned in the plane of the crest, shown in the same view as I. (K) Vector field of σ_3 in the medial aspect of the fibular head, in medial view. (L) Geometric representation of cancellous bone architecture in the fibular head of *Allosaurus* and tyrannosaurids (cf. Part I), in the same view as K.

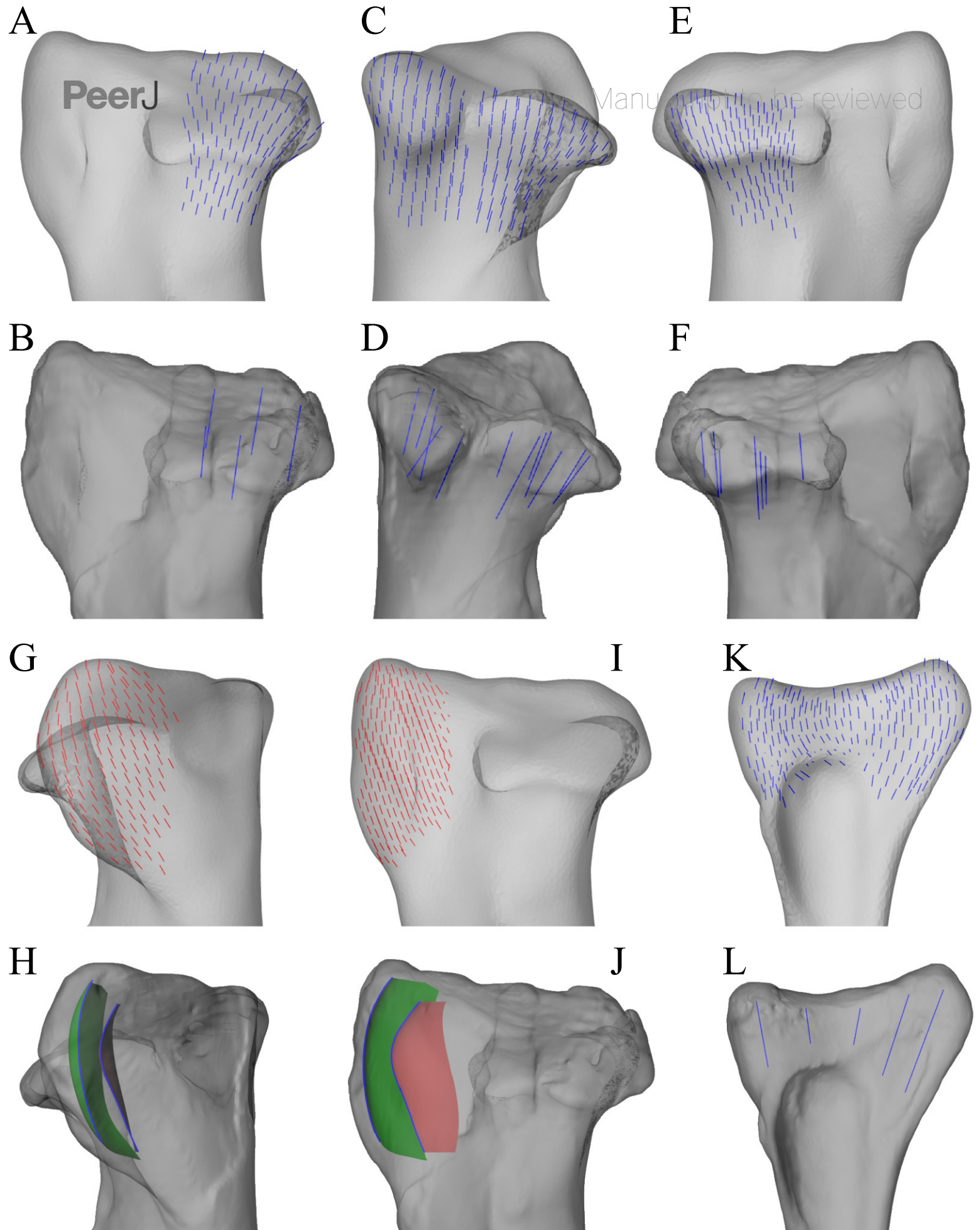


Figure 8(on next page)

Principal stress trajectories for the proximal femur in the solution posture of ' Troodon ', compared with observed cancellous bone fabric.

(A, B) Vector field of σ_3 in the femoral head, shown as 3-D slices parallel to the coronal plane (A, in anterior view) and sagittal plane (B, in medial view). (C, D) Vector field of u_1 in the femoral head, in the same views as A and B, respectively (cf. Part I) . (E) Comparison of the mean direction of σ_3 in the femoral head (blue) and the mean direction of u_1 (red), plotted on an equal-angle stereoplot with northern hemisphere projection. Inset shows location of region for which the mean direction of σ_3 was calculated. (F, G) Vector field of σ_3 under the greater trochanter, shown as 3-D slices parallel to the coronal plane (F, in posterior view) and sagittal plane (G, in lateral view). (H, I) Vector field of u_1 under the greater trochanter, shown in the same views as F and G, respectively (cf. Part I) . (J) Vector field of σ_1 in the lesser trochanter, shown in oblique anterolateral view. (K) Vector field of u_1 in the lesser trochanter, shown in the same view as J for both specimens studied (cf. Part I) .

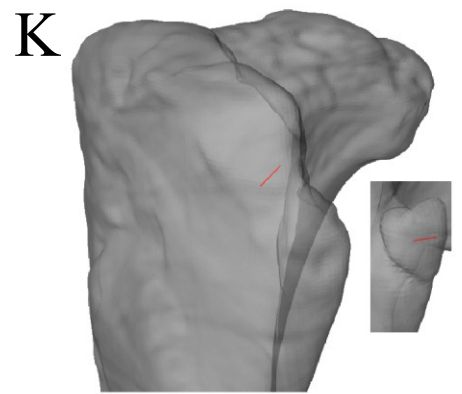
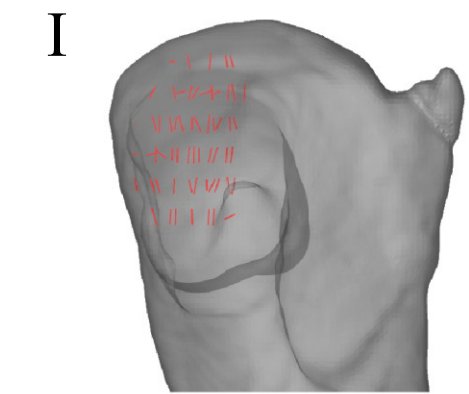
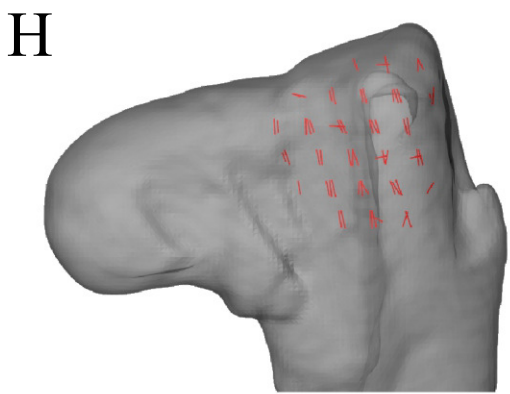
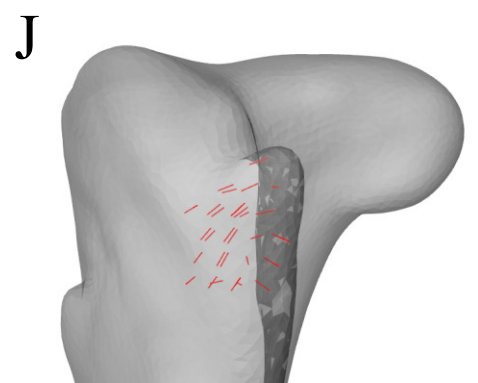
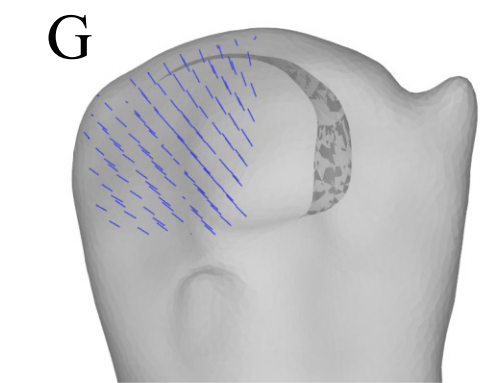
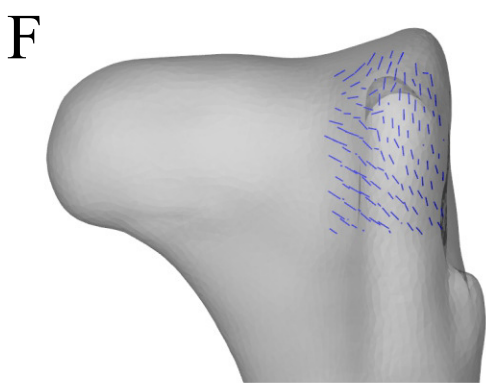
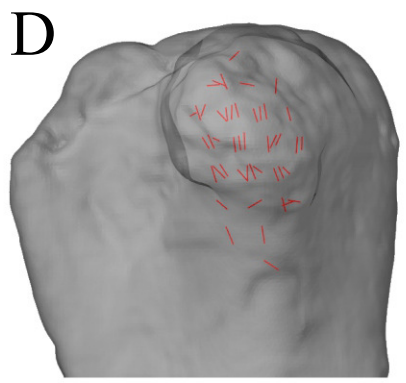
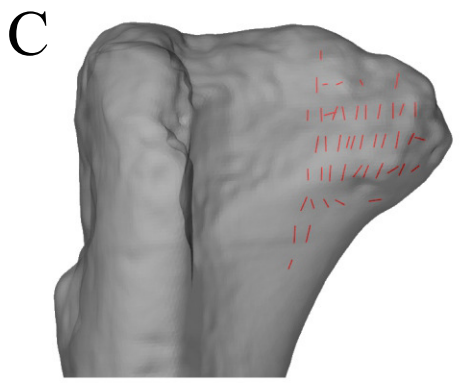
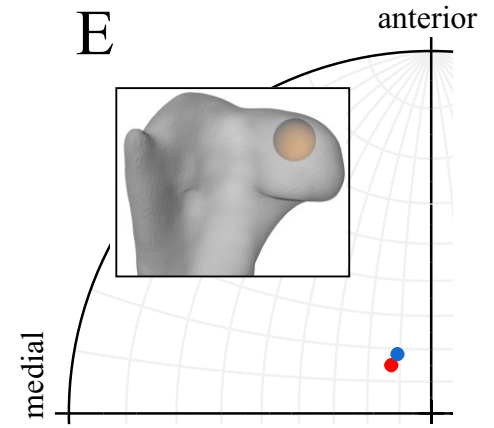
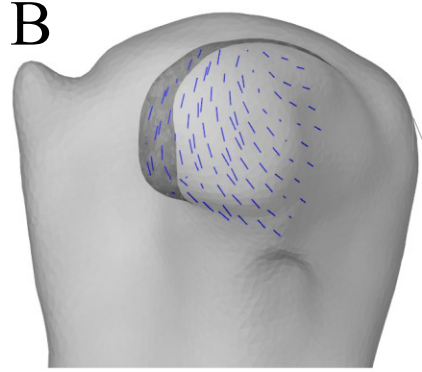
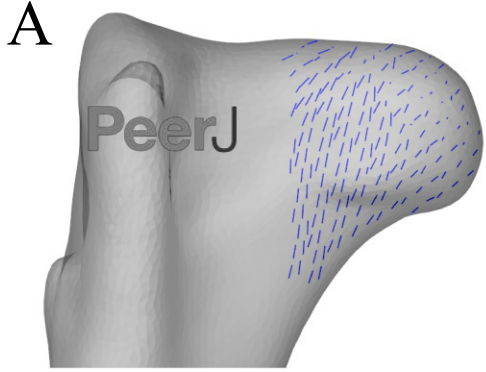


Figure 9(on next page)

Principal stress trajectories for the distal femoral condyles in the solution posture of 'Troodon', compared with observed cancellous bone fabric.

(A) Vector field of σ_3 in the lateral condyle, shown as a 3-D slice parallel to the sagittal plane. (B) Vector field of u_1 in the lateral condyle, shown in the same view as A (cf. Part I). (C) Vector field of σ_3 in the medial condyle, shown as a 3-D slice parallel to the sagittal plane. (D) Vector field of u_1 in the medial condyle, shown in the same view as C (cf. Part I). (E) Comparison of the mean direction of σ_3 in the medial condyle (blue) and the mean direction of u_1 (red), plotted on an equal-angle stereoplot with southern hemisphere projection. This shows that in the solution posture the mean direction of σ_3 was of the same general azimuth as the mean direction of u_1 , but was markedly more posteriorly inclined. Inset shows location of region for which the mean direction of σ_3 was calculated.

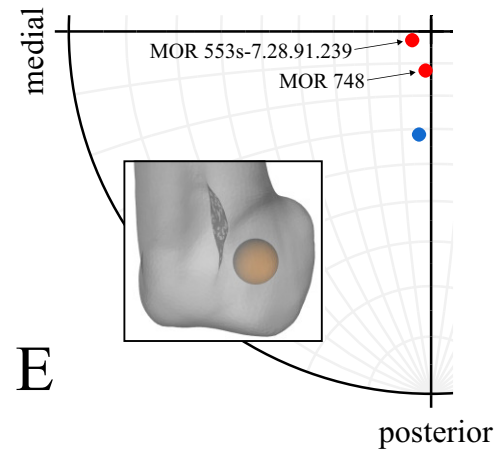
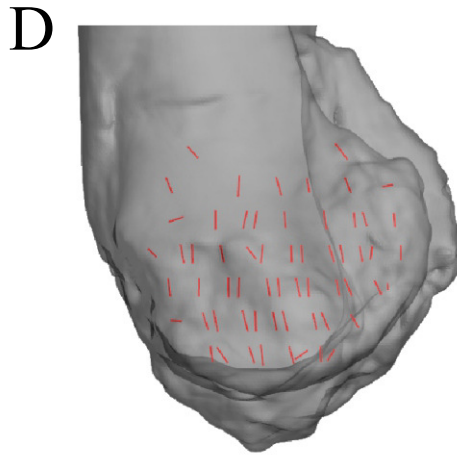
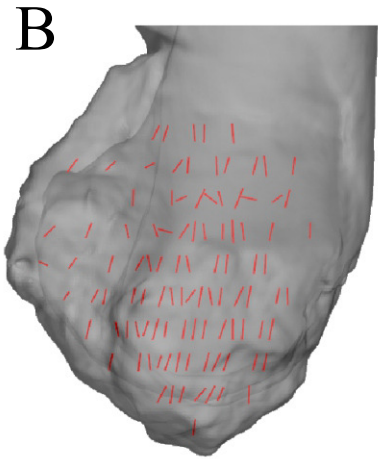
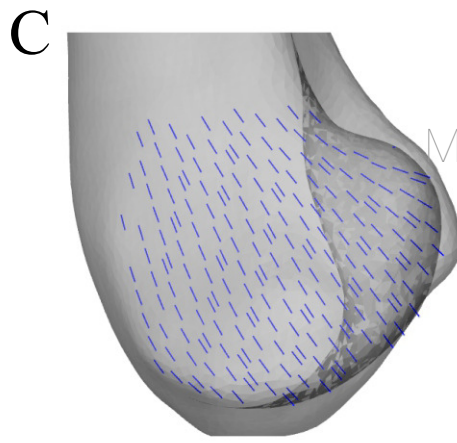
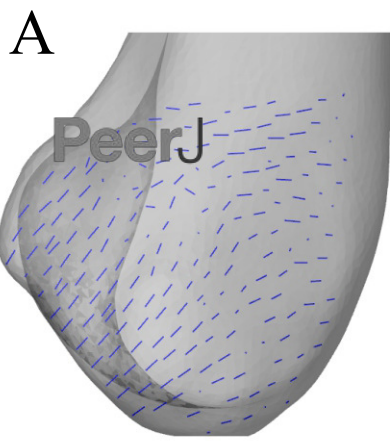


Figure 10(on next page)

Principal stress trajectories for the tibia and fibula in the solution posture for ' Troodon ', compared with observed cancellous bone fabric.

(A) Vector field of σ_3 in the medial tibial condyle, shown as a 3-D slice through the middle of the condyle and parallel to the sagittal plane, in medial view. (B) Vector field of u_1 in the medial tibial condyle, in the same view as A (cf. Part I) . (C) Vector field of σ_3 in the medial and lateral tibial condyles, shown as 3-D slices through the middle of the condyles and parallel to the coronal plane, in posterior view. (D) Vector field of u_1 in the medial and lateral tibial condyles , in the same view as C (cf. Part I) . (E) Vector field of σ_3 in the lateral tibial condyle, shown as a 3-D slice through the middle of the condyle and parallel to the sagittal plane, in lateral view. (F) Vector field of u_1 in the lateral tibial condyle, in the same view as E (cf. Part I) . (G) Vector field of σ_1 in the cnemial crest, shown as a 3-D slice parallel to the coronal plane, in anterior view. (H) Vector field of u_1 in the cnemial crest, in the same view as G (cf. Part I) . (I) Vector field of σ_1 in the cnemial crest, shown as a 3-D slice parallel to the sagittal plane, in medial view. (J) Vector field of u_1 in the cnemial crest, in the same view as I (cf. Part I) . (K) Vector field of σ_1 in the lateral fibular head, in lateral view. (L) Vector field of σ_3 in the medial fibular head, in medial view (reversed). (M) Vector field of u_1 in the fibular head, in the same view as K (cf. Part I) .

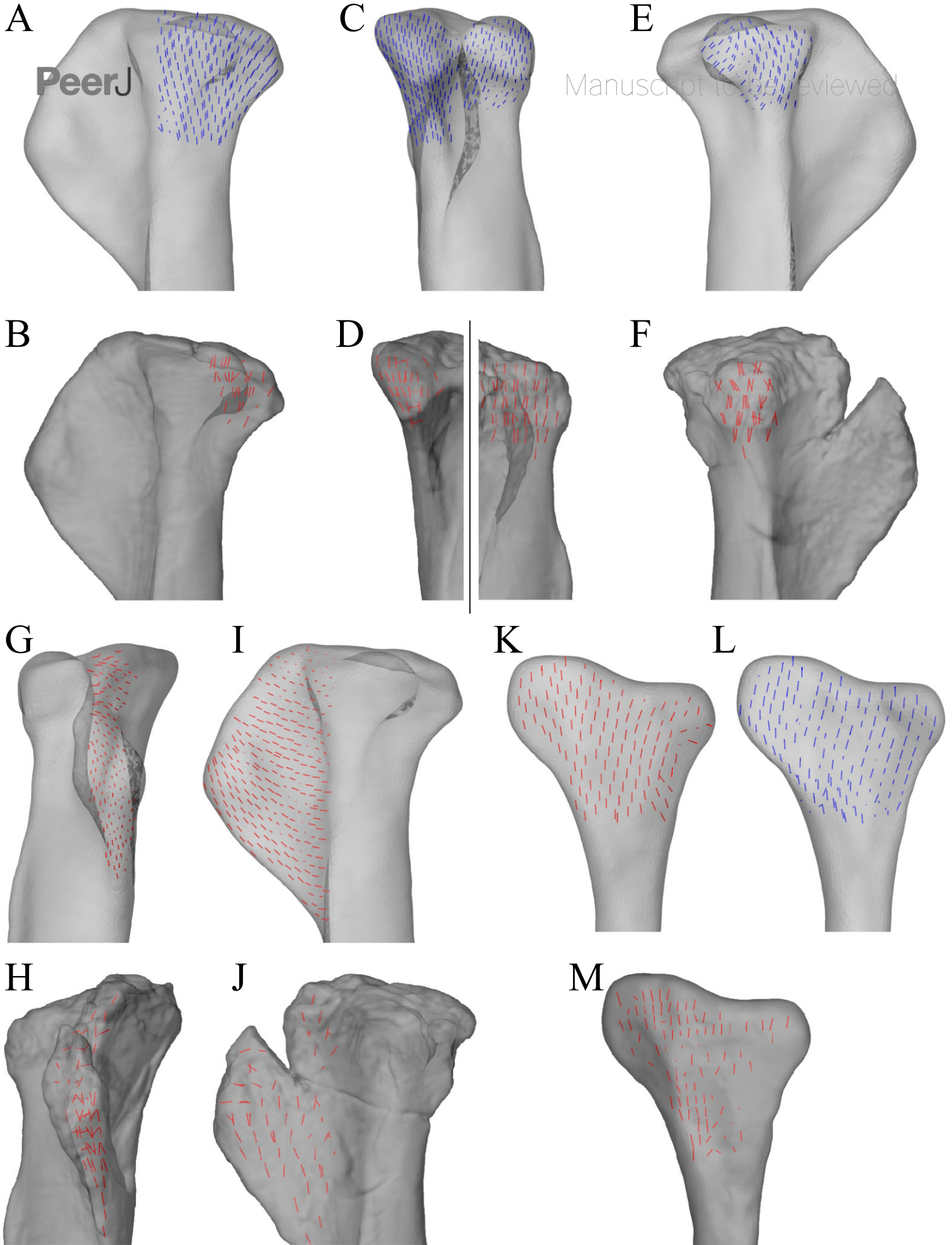
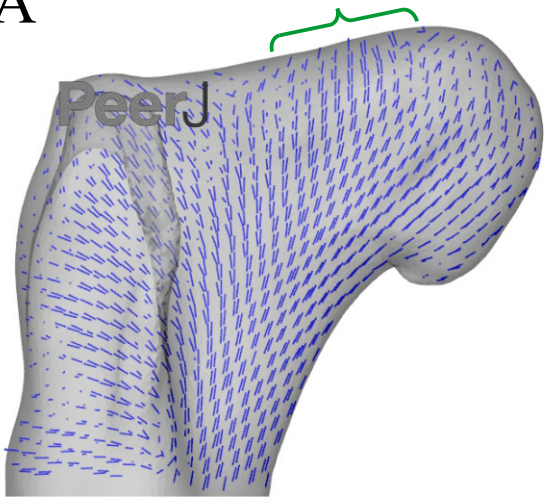


Figure 11(on next page)

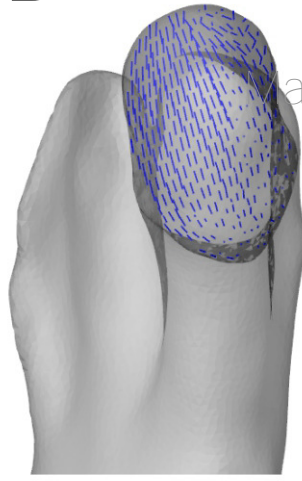
Principal stress trajectories for the proximal femur of *Daspletosaurus* in the two variations in hip articulation tested.

(A) Vector field of σ_3 in the first variation tested, shown as a 3-D slice parallel to the coronal plane and through the middle of the femoral head. (B) Vector field of σ_3 in the first variation tested, shown as a 3-D slice parallel to the sagittal plane and through the apex of the femoral head. (C) Vector field of σ_3 in the second variation tested, shown as a 3-D slice parallel to the coronal plane and through the middle of the femoral head. (D) Vector field of σ_3 in the second variation tested, shown as a 3-D slice parallel to the sagittal plane and through the apex of the femoral head. A and C are in anterior view, B and D are in medial view. Note in particular how the trajectory of σ_3 projects towards the more cylindrical part of the femoral head, lateral to the apex (green braces); compare to Fig. 5A,B,E,F. Also note in **C** how σ_3 has a strong medial component near the apex of the head.

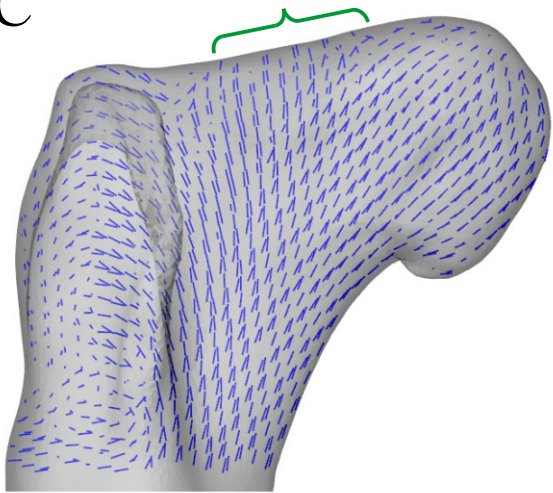
A



B



C



D

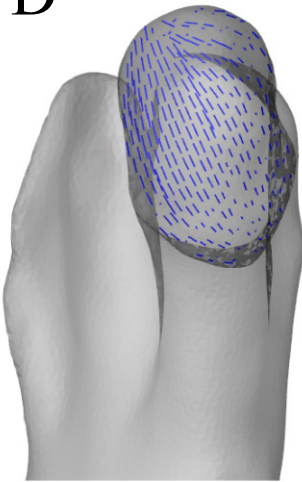


Figure 12(on next page)

Comparison of parameters related to posture, extracted from the solution postures of the three species modelled: Daspletosaurus ('D'), Troodon ('T') and the chicken ('C').

(A) Schematic illustration of the solution postures retrieved for the three species, along with the location of the whole-body centre of mass (black and white disc). (B) Whole-body centre of mass location anterior to the hips, normalized to total leg length. (C) Degree of crouch for each species, both as measured from the solution posture, as well as empirically predicted from the data reported by Bishop et al. (in review-a). (D) Angles of the hip and knee joints. The hip extension angle is expressed relative to the horizontal, whereas the knee flexion angle is expressed relative to the femur. (E) Long-axis rotation and adduction-abduction of the hip joint. Positive values indicate external rotation and abduction (respectively), whereas negative values indicate internal rotation and adduction (respectively).

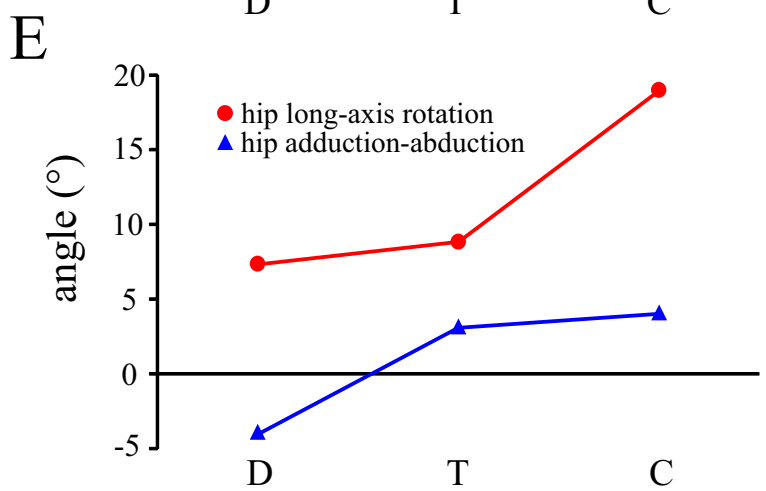
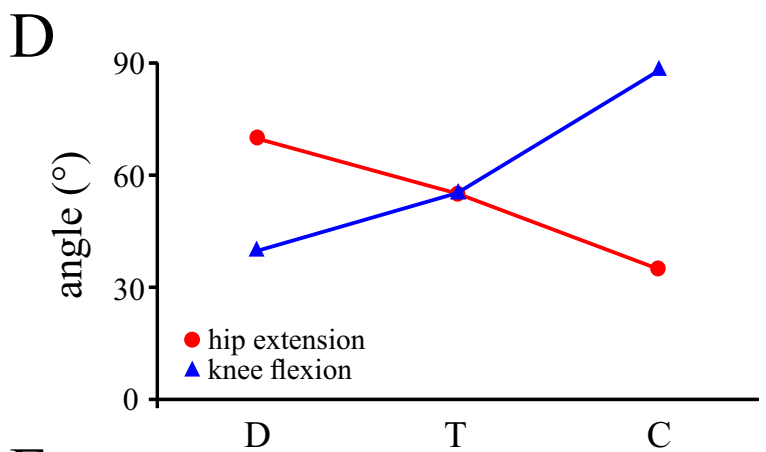
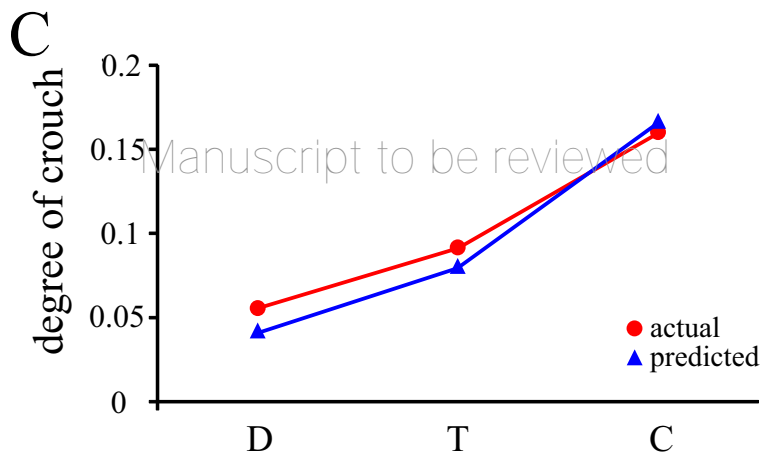
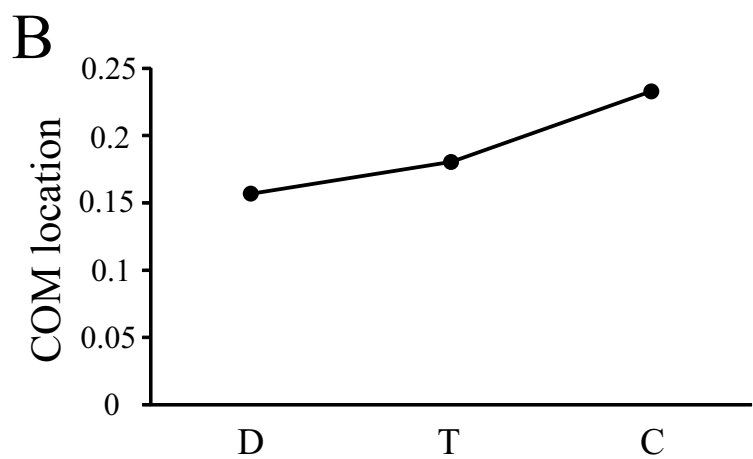
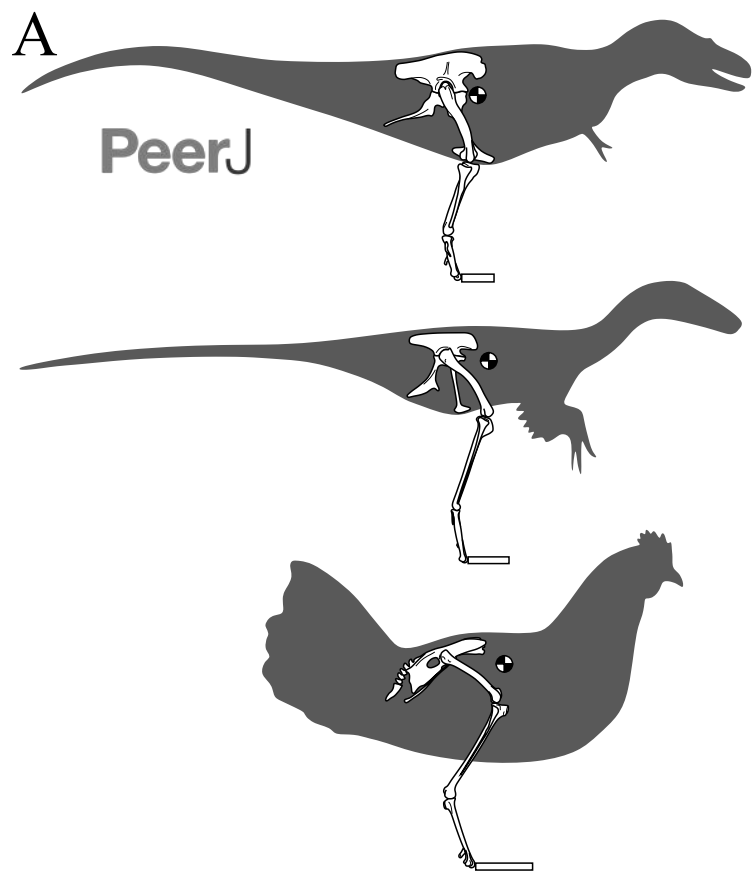


Figure 13(on next page)

Comparison of parameters related to bone loading mechanics and muscular support, extracted from the solution postures of the three species modelled: Daspletosaurus ('D'), 'Troodon' ('T') and the chicken ('C').

(A) Orientation of the neutral axis of bending and the orientation of principal stresses (σ_1 and σ_3) relative to the femur long-axis, both measured at mid-shaft. Insets show the neutral axis with respect to the mid-shaft cross-section, as well as anatomical directions (A, anterior; P, posterior; M, medial; L, lateral). (B) Ratio of maximum shear to bending stress in the femoral mid-shaft. (C) Normalized moments of hip abductor and medial rotator muscles. The hip abductor for all species is the iliofemoralis externus (activation set to zero in the chicken; see Part II). In Daspletosaurus and 'Troodon', the medial rotators are the iliotrochantericus caudalis and puboischiofemorales internus 1 et 2; in the chicken, they are the iliotrochanterici caudalis et medius. (D) Oblique anterolateral view of the hip of Daspletosaurus, showing the abductor and medial rotator muscles (colour codes as in C).

